Atomic mechanism of $\{10\bar{1}2\}$ twin growth in Mg and Ti by phonon calculations

Keiyu Mizokami

2022

Contents

Chapter 1

General Introduction

1.1 Hexagonal deformation twinning

Hexagonal materials with hexagonal close-packed (HCP) crystal structure, such as Mg and Ti, are attractive due to their high specific strength compared with traditional structural materials and are widely used as structural materials in many industries. Mg and its alloys are promising next-generation light-weight structural materials for reducing the weight of the vehicles and increase their efficiency and reduce the amount of greenhouse gas [1]. Ti and its alloys attract wide application in aerospace, chemical industry and medical implants because of excellent corrosion resistance and good biocompatibility in addition to preferable physical and mechanical properties [2]. Understanding the individual defects and the interactions between these defects at the atomic scale is significant for materials engineering.

Deformation twinning in HCP metals plays a crucial role as one of the plastic deformation modes along the $\langle c \rangle$ axis, because the dominant slip systems for Mg and Ti are $\langle a \rangle$ basal slip and $\langle a \rangle$ prism slip, respectively [3–5], which have $\frac{1}{3}\langle 1\bar{2}10 \rangle$ burgers vectors, and they are the main carriers of plastic deformation in HCP metals but cannot accommodate any strain along the

$\langle c \rangle$ axis. Even though HCP crystal structure is one of the three most common crystal structures in structural materials along with FCC and BCC crystal structures, its deformation modes have higher complexity. This comes from the fact that HCP crystal structure has hexagonal lattice and there are two atoms in the primitive cell where FCC and BCC crystal structures are cubic and a single atom is included in the primitive cell. Owing to this structure feature, the atomic motions during twin growth in HCP metals do not merely follow shear strain (affine transformation), but atomic shuffling (non-affine transformation) must be occurred [6, 7]. Therefore, it is impossible to explain deformation twinning in HCP metals with simple dislocation twinning. From this complexity, the twin nucleation and growth mechanisms in HCP metals are still not clear and sincerely investigated by many researchers. Among several hexagonal twinning modes that could be active, $\{10\bar{1}2\}$ twinning mode has the smaller twinning shear values [8] and the most commonly observed twinning mode in experiments in HCP materials [9, 10]. While the crystallography of the deformation twinning is well asserted [6, 7], the atomic-scale mechanisms of twin nucleation and its growth are still the object of active research [11–16].

From atomic point of view, $\{10\bar{1}2\}$ twin boundary is not fully coherent but often deviates from theoretical one by exhibiting steps [17], especially at twin tips [18]. Recently, atomic-scale $\{10\bar{1}2\}$ twin growth process was directly observed in Re nanocrystals by in-situ high resolution transmission electron microscopy (HRTEM) [19]. They found out the migration of twin boundary is proceeded by the dual steps sweeping on the twin boundary during detwinning process as shown in Fig.1.1. The dual steps meditated twin growth mechanism has been already proposed by Pond, Hirth, Serra and Bacon [11,12]. They considered the twin boundary migration is meditated by the steps formed at the interface and introduced the concept "disconnection" to describe the interfacial defects mediating twin boundary migration. This interfacial defects called as disconnection have both dislocation and step character. With this newly introduced concept, they proposed twin thickening process with

disconnection gliding on the twin boundary. However, in this disconnection model they do not clearly denote how atoms around the twin boundary rearrangement occurs during twin boundary migration when external stress is applied to the twin boundary. On the other hand, some other researchers propose atomic scale twin growth models in $\{10\bar{1}2\}$ coherent twin boundary (CTB) which describe the pathway of each atom during twin boundary migration [13–16]. However, these models are based on topological analysis and atomic shuffles are determined from the concept that "the shuffle magnitudes should be small" remarked by Bilby *et al.* [6], and their validity is not discussed based on energetic point of view. Moreover, the $\{10\bar{1}2\}$ twin growth mechanism observed by in-situ HRTEM in Re, in which the dual steps on the twin boundary play a key role, is beyond their scope.

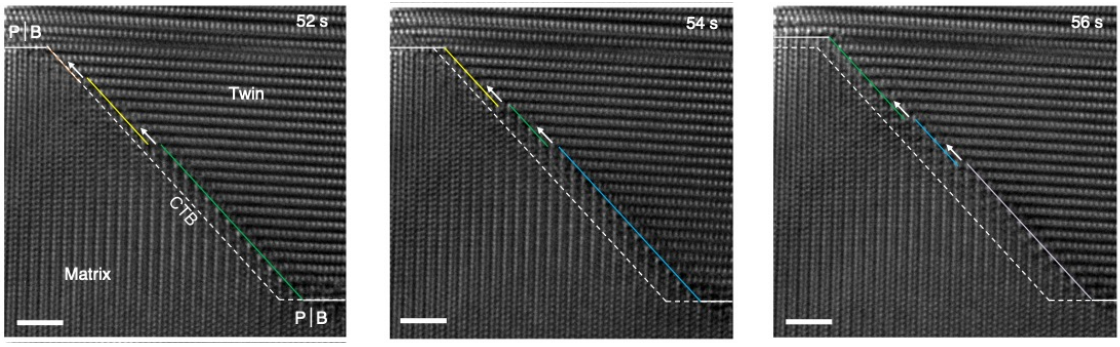

Figure 1.1: Sequential HRTEM snapshots for $\{10\bar{1}2\}$ CTB propagation by the dual steps sweeping on the twin boundary during detwinning process in Re [19].

On the other hand, some researchers consider deformation twinning as a special type of stress driven transformation and the atomic rearrangement during twin boundary migration is characterized by collective movement of atoms [15, 20]. In this point of view, phonons which represent atomic vibrations in crystal play a central role. Therefore, we decided to conduct phonon calculations toward $\{10\bar{1}2\}$ twin boundary structures and analyze the change of phonon state during applying

shear stress. External stress is expected to change potential energy surface and affect the phonon states while the equilibrium positions of atoms move, and finally some specific phonon modes are expected to show imaginary frequencies which means the sheared structure is dynamically unstable. Our strategy provides the initial motion from dynamically unstable structure to the dynamically stable structure under the applied shear stress, because we can get the unstable vibration directions of atoms from the eigenvectors of the imaginary phonon modes. As far as we know, Togo has firstly studied phonon structure change while applying shear stress using Ti $\{10\bar{1}2\}$ twinning mode and revealed a characteristic phonon mode that exhibits structural instability under certain shear and proposed the pathway of atomic rearrangement from this soft phonon mode [20], but his calculations do not provide phonon structures around twin boundary and their change.

From these backgrounds, we have decided to study the phonon structures of Mg and Ti $\{10\bar{1}2\}$ twin boundary and their change during applying shear stress. As for $\{10\bar{1}2\}$ twin boundary structures, we first study coherent twin boundaries because of their structural simplicity in Chapter. 2. Then, we consider the dual step introduced $\{10\bar{1}2\}$ twin boundaries as more actual models in Chapter. 3. In this thesis, we show the atomic rearrangement process around $\{10\bar{1}2\}$ twin boundary from phonon calculations and imaginary phonon mode analyses.

1.2 Overview

In Chapter 2, atomic pathways during the twin growth of $\{10\bar{1}2\}$ CTB in Mg and Ti are provided from a series of phonon calculations. We first describe the method of building $\{10\bar{1}2\}$ CTB structure from dichromatic pattern [21] in Session 2.2. Then, theoretical backgrounds for lattice dynamics and imaginary phonon mode are reviewed in Session 2.3. Throughout Chapter 2, we use first-principles phonon calculations toward $\{10\bar{1}2\}$ CTB in Mg and Ti with Vienna *ab initio*

simulation (VASP) [22–25] and phonopy [26] packages. The computational details for calculations are described in Session 2.4. In Session 2.5, we provide phonon structures under zero shear stress and phonon structure changes under the applied shear stresses. Finally, we provide the atomic motions during twin growth based on the eigenvectors of the characteristic phonon modes which have imaginary frequencies under a certain shear stress.

In Chapter 3, we select the dual step introduced $\{10\bar{1}2\}$ twin boundary structure as a more actual case than CTB structure and the atomic pathways during the twin growth are provided from a series of phonon calculations. We first describe the method of building the dual step introduced $\{10\bar{1}2\}$ twin boundary structure from dichromatic pattern [21] in Session 3.2. Because the simulation cells are much larger than CTB structures and it is impossible to conduct first-principles phonon calculations, we use machine learning interatomic potentials (MLIP) for phonon calculations. The theoretical backgrounds for MLIP is reviewed in Section 3.3. Then, computational details for calculations are described in Session 3.4. In Session 3.5, we provide the phonon structure changes of dual step introduced twin boundary structures in Mg and Ti and the atomic pathways associated with dual step gliding are provided from the imaginary phonon mode analyses.

Chapter 2

Atomic Mechanism of Twin Growth in Mg and Ti $\{10\bar{1}2\}$ Coherent Twin Boundaries

2.1 Introduction

As remarked in general introduction, we consider deformation twinning is a special type of stress driven transformation and the atomic rearrangement during twin boundary migration is characterized by collective movement of atoms around twin boundary. From this point of view, phonon structures around $\{10\bar{1}2\}$ twin boundary and their change by external shear stress should be important to understand twin boundary migration. As far as we know, no other research of twin growth considers it based on lattice dynamics, though some studies conduct phonon calculations toward $\{10\bar{1}2\}$ coherent twin boundary (CTB) structures to check their dynamical stability [27,28]. Therefore, we decide to conduct a series of phonon calculations toward Mg and Ti $\{10\bar{1}2\}$ CTB structures while applying external shear stresses and analyze the phonon structure changes.

CTB is the simplest structural version of twin boundary, where the twin lattice is exactly a mirror reflection of the matrix lattice in $\{10\bar{1}2\}$ twinning mode. However, even with the use of $\{10\bar{1}2\}$ CTB

model in HCP, the twin growth mechanism is still complicated because $\{10\bar{1}2\}$ crystallographic plane is not flat but corrugated in nature and this necessitates additional atomic motions (shuffle), apart from shear. In the last two decades, huge amount of efforts have been devoted to studying the structures and energetics of $\{10\bar{1}2\}$ CTBs in HCP Mg and Ti using a variety of simulation methods such as molecular statics (MS) [29], molecular dynamics (MD) [30], and first-principles density functional theory (DFT) [31–34], but many of them dedicate to discuss structural stability based on energetics, and they do not discuss about twin growth which accompanies atomic rearrangement around twin boundary. On the other hand, some papers consider the $\{10\bar{1}2\}$ twin boundary migration mechanisms from atomic point of view, but they are based on the observation of HRTEM [16] or the simple topological calculations [14, 15], and they do not clarify what is the trigger of the twin boundary migration.

In this chapter, we provide phonon structure changes by external shear stress and show some specific imaginary phonon modes play a key role in the twin boundary migration in Mg and Ti $\{10\bar{1}2\}$ CTB. In Section 2.2, the method of building $\{10\bar{1}2\}$ CTB introduced structure is discussed. The necessary backgrounds for lattice dynamics and the computational details for first-principles phonon calculations are reviewed in Section 2.3 and Section 2.4. In Section 2.5, the phonon structures for the Mg and Ti $\{10\bar{1}2\}$ CTBs and their sheared structures are provided and the atomic rearrangement accompanied by twin boundary migration is clarified.

2.2 Modeling $\{10\bar{1}2\}$ coherent twin boundary

Twinning modes are historically characterized by a set of four twinning elements defined by the classical theory of deformation twinning, which are $\boldsymbol{\eta}_1$ and $\boldsymbol{\eta}_2$ invariant directions, and K_1 and K_2 invariant planes [6]. FIG.2.1 shows the invariant plane relations between matrix and twin, where

its half upper part is homogeneously sheared by twinning shear strain s^{t} into twin. K_2 and K_2', and $\boldsymbol{\eta}_2$ and $\boldsymbol{\eta'}_2$ are crystallographic equivalent planes and directions, respectively. We define the shear plane P and three vectors $\boldsymbol{m}$, $\boldsymbol{k}_1$ and $\boldsymbol{k}_2$ which are normal to P, K_1 and K_2 planes respectively. The set of the basis vectors of HCP crystal structure is given as $[\boldsymbol{a}^{\mathrm{h}}, \boldsymbol{b}^{\mathrm{h}}, \boldsymbol{c}^{\mathrm{h}}]$.

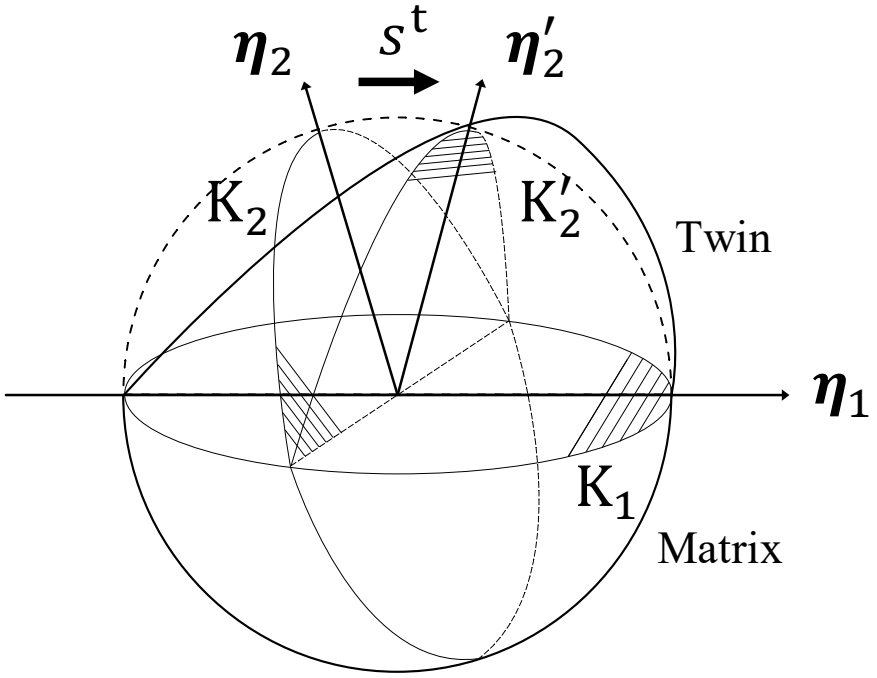

Figure 2.1: The relations of invariant planes and directions between matrix and twin. The sphere represents matrix and its half upper part homogeneously is sheared into a half-ellipsoid (twin), which is first represented by Hall [35].

For $\{10\bar{1}2\}$ twinning mode, four twinning elements and corresponding twinning shear strain are given as $K_1 = \{10\bar{1}2\}$, $K_2 = \{10\bar{1}\bar{2}\}$, $\boldsymbol{\eta}_1 = \langle 10\bar{1}\bar{1}\rangle$, $\boldsymbol{\eta}_2 = \langle 10\bar{1}1\rangle$ and $s^{\mathrm{t}} = \frac{|3-\gamma^2|}{\sqrt{3}\gamma}$ with $\gamma = c^{\mathrm{h}}/a^{\mathrm{h}}$ [7,8]. To represent the $\{10\bar{1}2\}$ twinning mode for calculations, it is convenient to retake the hexagonal lattice by its extended unit cell, which we call as parent and its basis vectors are given as $[\boldsymbol{a}^{\mathrm{m}}, \boldsymbol{b}^{\mathrm{m}}, \boldsymbol{c}^{\mathrm{m}}]$. The basis vectors $[\boldsymbol{a}^{\mathrm{m}}, \boldsymbol{b}^{\mathrm{m}}, \boldsymbol{c}^{\mathrm{m}}]$ are chosen so that the conditions $\boldsymbol{a}^{\mathrm{m}} \parallel \boldsymbol{m}$, $\boldsymbol{b}^{\mathrm{m}} \parallel \boldsymbol{\eta}_1$ and $\boldsymbol{c}^{\mathrm{m}} \parallel \boldsymbol{\eta}_2$ are fulfilled and they make a right-handed system. In this condition, the transformation matrix from

hexagonal lattice to parent lattice $\boldsymbol{M}$ can be written as,

$$[\boldsymbol{a}^{\mathrm{m}}, \boldsymbol{b}^{\mathrm{m}}, \boldsymbol{c}^{\mathrm{m}}] = [\boldsymbol{a}^{\mathrm{h}}, \boldsymbol{b}^{\mathrm{h}}, \boldsymbol{c}^{\mathrm{h}}]\boldsymbol{M}, \tag{2.1}$$

with

$$\boldsymbol{M} = \begin{pmatrix} 0 & 2 & \bar{2} \\ \bar{1} & 1 & \bar{1} \\ 0 & 1 & 1 \end{pmatrix}, \tag{2.2}$$

where the bars on the matrix elements denote the negative numbers. Twinning operation is either a reflection in K_1 plane (Type I), or a rotation of π along the $\boldsymbol{\eta}_1$ direction (Type II). As for $\{10\bar{1}2\}$ twinning mode, it is simultaneously of type I and Type II because both operations are equivalent [7]. In this study, the twin lattice is generated by applying reflection operation on K_1 plane of the parent lattice. The set of the basis vectors of the twin lattice is given as $[\boldsymbol{a}^{\mathrm{t}}, \boldsymbol{b}^{\mathrm{t}}, \boldsymbol{c}^{\mathrm{t}}]$. With these basis vectors, the relation between matrix lattice and twin lattice of $\{10\bar{1}2\}$ twinning mode becomes clear as shown in Fig.2.2.

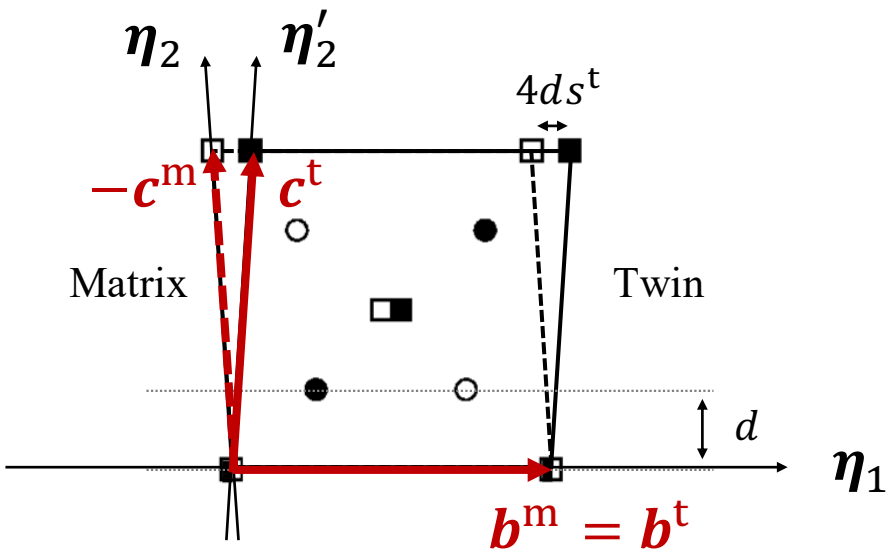

Figure 2.2: The relations of invariant planes and directions between matrix and twin lattice. Matrix is sheared by s^{t} into the twin. The white and the black points represent the hexagonal lattice points of matrix and twin. The squared dots are half shifted along the vertical direction of paper compared with the circled dots. The notation d represents plane interval for $\{10\bar{1}2\}$ planes and, four $\{10\bar{1}2\}$ planes are included in the unit lattices $[\boldsymbol{a}^{\mathrm{m}}, \boldsymbol{b}^{\mathrm{m}}, \boldsymbol{c}^{\mathrm{m}}]$ and $[\boldsymbol{a}^{\mathrm{t}}, \boldsymbol{b}^{\mathrm{t}}, \boldsymbol{c}^{\mathrm{t}}]$.

FIG.2.3 shows the matrix lattice points (white dots) and the twin lattice points (black dots) which are generated by mirror operation at a specific $\{10\bar{1}2\}$ plane in matrix, which is called dichromatic pattern [21, 36]. By this operation, $\{10\bar{1}2\}$ twin boundary is generated and the lattice points on the twin boundary where parent and twin lattice points overlap are called grey lattice points. From this dichromatic pattern, unit lattice used in this work is extracted so that the extracted unit lattice contains ten layers of $\{10\bar{1}2\}$ plane both in parent and twin lattice as represented with black dotted line in Fig.2.3. Let the basis vectors of the newly defined unit lattice be given as $[\boldsymbol{a}, \boldsymbol{b}, \boldsymbol{c}]$, then they are represented as,

$$\boldsymbol{a} = \boldsymbol{a}^{\mathrm{p}} = \boldsymbol{a}^{\mathrm{t}}, \qquad \boldsymbol{b} = \boldsymbol{b}^{\mathrm{p}} = \boldsymbol{b}^{\mathrm{t}}, \qquad \boldsymbol{c} = \frac{11}{4}(\boldsymbol{c}^{\mathrm{t}} - \boldsymbol{c}^{\mathrm{m}}). \tag{2.3}$$

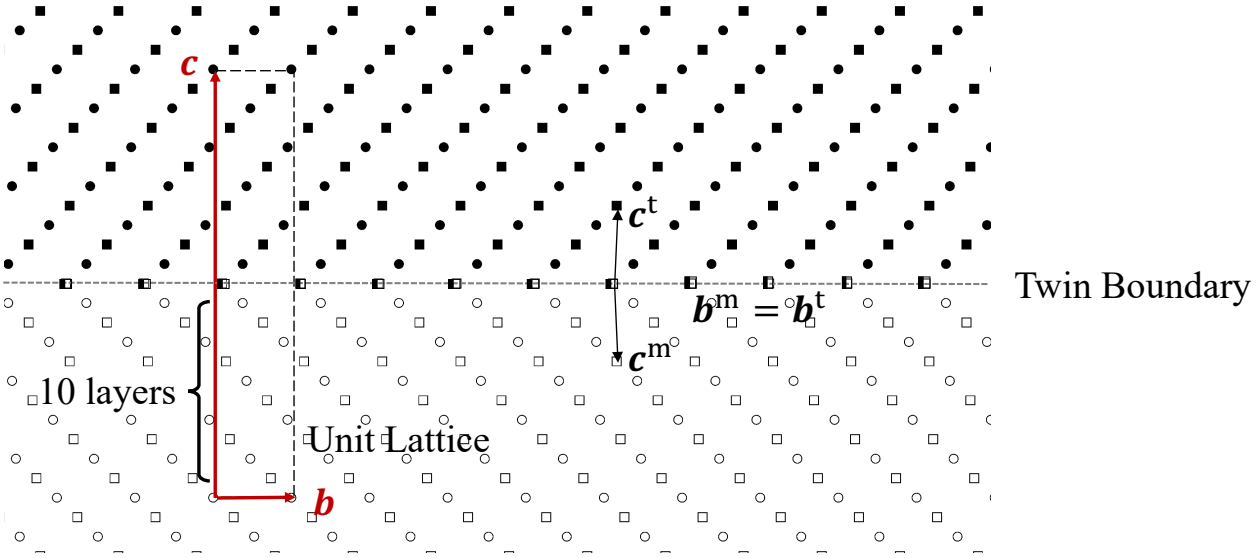

Figure 2.3: Dichromatic pattern of $\{10\bar{1}2\}$ CTB is shown. The white and the black points represent the hexagonal lattice points of matrix and twin. Twin lattice points are generated by mirror operation toward the top $\{10\bar{1}2\}$ plane in matrix and this plane becomes twin boundary as shown in figure. The unit lattice used in this work is represented by black dashed line. The squared dots are half shifted along the vertical direction of paper compared with circled dots.

The unit cell is defined by embedding atoms against the hexagonal lattice points in the unit lattice represented in Fig.2.3 as shown in Fig.2.4, which is called as dichromatic complex in some papers [21, 37]. For the lattice points on the twin boundary, atom pairs are projected onto the twin boundary. In order to fulfill the periodic condition along c axis, the atom pairs on the top (and equivalently on the bottom) of $\{10\bar{1}2\}$ plane is also projected onto the plane. As a result, in addition to $\{10\bar{1}2\}$ twin boundary placed in the middle of the unit cell, the additional twin boundary is generated at the top (and equivalently at the bottom) of the unit cell as represented in Fig.2.5. The unit cell contains the total twenty-two $\{10\bar{1}2\}$ planes where there are ten planes in matrix and twin, and two twin boundaries. Therefore, there are forty-four atoms in the unit cell because atom pairs belong for each plane in the unit cell.

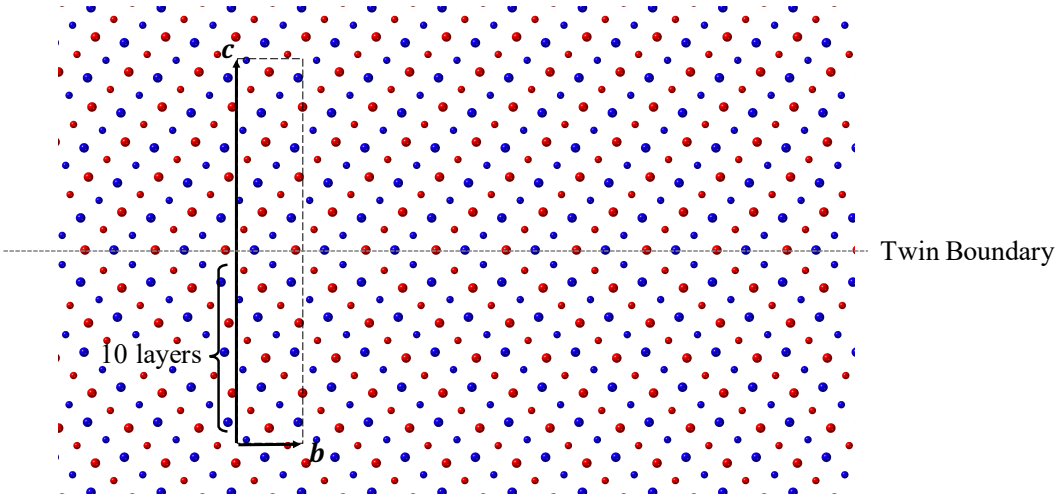

Figure 2.4: Dichromatic complex is shown where the atom pair of HCP primitive cell is embedded toward each lattice points of dichromatic pattern represented in Fig.2.3. The atom pair is represented with red and blue spheres. The smaller spheres are half shifted along the vertical direction of paper compared with bigger spheres.

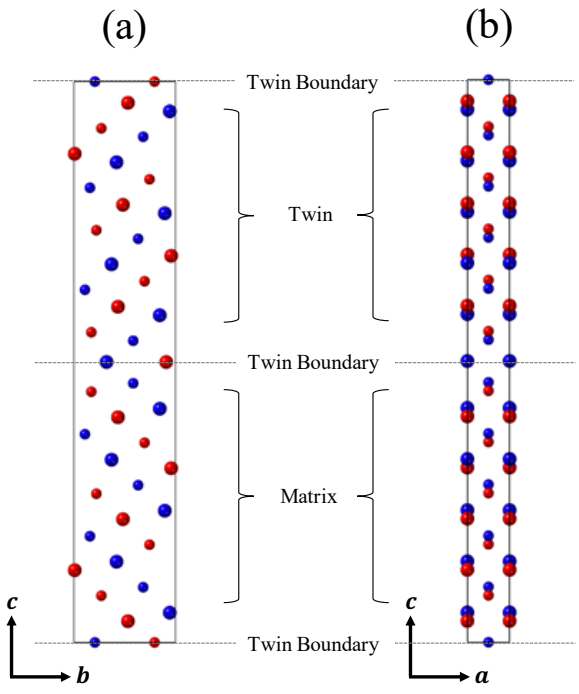

Figure 2.5: The extracted unit cell containing $\{10\bar{1}2\}$ twin boundary at the top, middle and bottom is shown. (a) and (b) is the unit cell viewed along a axis and b axis, respectively. The unit cell contains the total twenty-two $\{10\bar{1}2\}$ planes where there are ten planes in matrix and twin, and two twin boundaries.

2.3 Theoretical backgrounds for lattice dynamics and imaginary phonon mode

In this section, theoretical backgrounds for lattice dynamics [38–41] are reviewed and the concept of imaginary phonon mode is introduced. Let the primitive cell of crystal structure be defined with a set of basis vectors $[\boldsymbol{a}_1, \boldsymbol{a}_2, \boldsymbol{a}_3]$, then lattice points can be written as,

$$\boldsymbol{l} = l_1\boldsymbol{a}_1 + l_2\boldsymbol{a}_2 + l_3\boldsymbol{a}_3 \tag{2.4}$$

where l_1, l_2, l_3 are integers. With these lattice points, the equilibrium position of the κth atom in the lth unit cell is defined as $\boldsymbol{l} + \boldsymbol{\kappa}$, where $\boldsymbol{\kappa}$ is representing the position of κth atom from the reference lattice point. When the position of the κth atom in the lth unit cell is represented as $\boldsymbol{r}(\boldsymbol{l\kappa})$, the displacement vector $\boldsymbol{u}(\boldsymbol{l\kappa})$ is defined as

$$\boldsymbol{u}(\boldsymbol{l\kappa}) = \boldsymbol{r}(\boldsymbol{l\kappa}) - (\boldsymbol{l} + \boldsymbol{\kappa}). \tag{2.5}$$

In lattice dynamics theory, it is presumed that atoms vibrate around their equilibrium positions with small amplitudes. Under this assumption, the crystal potential energy $\mathscr{V}$ can be described as a Taylor series expansion with respect to atomic displacement $\boldsymbol{u}(\boldsymbol{l\kappa})$ as,

$$\mathscr{V} = \mathscr{V}_0 + \mathscr{V}_1 + \mathscr{V}_2 + \mathscr{V}_3 + \cdots, \tag{2.6}$$

where the zeroth order term $\mathscr{V}_0$ is constant and is unimportant for dynamical problems and can be set to zero, and the first order term $\mathscr{V}_1$ produces a force and must vanish in the equilibrium configuration. Therefore, the second and the higher order terms are important in dynamical

problems. In the harmonic approximation, crystal potential energy $\mathscr{V}_{\mathrm{H}}$ is defined by eliminating the third and the higher order terms as,

$$\mathscr{V}_{\mathrm{H}} \equiv \mathscr{V}_2 = \frac{1}{2} \sum_{\boldsymbol{l}\boldsymbol{\kappa}\alpha} \sum_{\boldsymbol{l}'\boldsymbol{\kappa}'\beta} \Phi_{\alpha\beta}(\boldsymbol{l}\boldsymbol{\kappa}, \boldsymbol{l}'\boldsymbol{\kappa}') u_\alpha(\boldsymbol{l}\boldsymbol{\kappa}) u_\beta(\boldsymbol{l}'\boldsymbol{\kappa}'), \tag{2.7}$$

where $\Phi_{\alpha\beta}(\boldsymbol{l}\boldsymbol{\kappa}, \boldsymbol{l}'\boldsymbol{\kappa}')$ is the second order force constants represented as,

$$\Phi_{\alpha\beta}(\boldsymbol{l}\boldsymbol{\kappa}, \boldsymbol{l}'\boldsymbol{\kappa}') = \frac{\partial^2 \mathscr{V}}{\partial u_\alpha(\boldsymbol{l}\boldsymbol{\kappa}) \partial u_\beta(\boldsymbol{l}'\boldsymbol{\kappa}')}. \tag{2.8}$$

For obtaining a general expression for lattice dynamics, periodic boundary condition is introduced as,

$$\boldsymbol{u}_{\boldsymbol{\kappa}}(\boldsymbol{l}) = \boldsymbol{u}_{\boldsymbol{\kappa}}(\boldsymbol{l} + N_1\boldsymbol{a}_1) = \boldsymbol{u}_{\boldsymbol{\kappa}}(\boldsymbol{l} + N_2\boldsymbol{a}_2) = \boldsymbol{u}_{\boldsymbol{\kappa}}(\boldsymbol{l} + N_3\boldsymbol{a}_3) \tag{2.9}$$

where N_1, N_2, N_3 are integers and they are large enough. This provides a mathematical scheme to avoid unimportant effects on the dynamical problem of an infinitely large crystal system. When the fourier transformation of $\boldsymbol{u}(\boldsymbol{l}\boldsymbol{\kappa})$ is considered under the periodic boundary condition, only discrete q-points in reciprocal space have non-zero value. These q-points can be represented as,

$$\boldsymbol{q} = \frac{2\pi n_1}{N_1}\boldsymbol{a}_1^* + \frac{2\pi n_2}{N_2}\boldsymbol{a}_2^* + \frac{2\pi n_3}{N_3}\boldsymbol{a}_3^* \qquad (0 \le n_i < N_i), \tag{2.10}$$

where $[\boldsymbol{a}_1^*, \boldsymbol{a}_2^*, \boldsymbol{a}_3^*]$ are the basis vectors of reciprocal lattice. With these q-points, the displacement vector $\boldsymbol{u}(\boldsymbol{l}\boldsymbol{\kappa})$ at a specific time t can be expanded into fourier series as,

$$u_\alpha(\boldsymbol{l}\boldsymbol{\kappa}, t) = \frac{1}{\sqrt{N m_\kappa}} \sum_{\boldsymbol{q}} U_\alpha(\boldsymbol{q}, \boldsymbol{\kappa}) \exp[i(\boldsymbol{q} \cdot \boldsymbol{r}(\boldsymbol{l}\boldsymbol{\kappa}) - \omega t)], \tag{2.11}$$

where m_κ is the mass of κth atom and N is the number of q-points, which can be written as,

$$N = N_1 N_2 N_3. \tag{2.12}$$

Let m be the number of atoms in the unit cell, the collective displacements from their equilibrium positions can be described in the $3mN$ dimension. Each atom obeys the Newton's motion equation as,

$$m_b \ddot{u}_\alpha(\boldsymbol{l\kappa}, t) = -\sum_{\boldsymbol{l'\kappa'}\beta} \Phi_{\alpha\beta}(\boldsymbol{l\kappa}, \boldsymbol{l'\kappa'}) u_\beta(\boldsymbol{l'\kappa'}, t). \tag{2.13}$$

The second order force constant Φ obeys two important symmetry relations. From the lattice translational symmetry, we have,

$$\Phi(\boldsymbol{l\kappa}, \boldsymbol{l'\kappa'}) = \Phi(\boldsymbol{0\kappa}, \boldsymbol{(l'-l)\kappa'}), \tag{2.14}$$

and from the result that there is no force on any atom when all the atoms are equally displaced, we have,

$$\Phi(\boldsymbol{l\kappa}, \boldsymbol{l\kappa}) = -\sum_{\boldsymbol{l'\kappa'} \neq \boldsymbol{l\kappa}} \Phi(\boldsymbol{l\kappa}, \boldsymbol{l'\kappa'}). \tag{2.15}$$

Using these symmetry relations, Eq.(2.13) can be expressed as,

$$m_b \ddot{u}_\alpha(\boldsymbol{l\kappa}, t) = -\sum_{\boldsymbol{l'\kappa'}\beta} \Phi_{\alpha\beta}(\boldsymbol{0\kappa}, \boldsymbol{l'\kappa'}) u_\beta(\boldsymbol{l'\kappa'}, t). \tag{2.16}$$

By substituting Eq.(2.11) into Eq.(2.16), we get,

$$\sum_{\boldsymbol{\kappa'}\beta} D_{\alpha\beta}(\boldsymbol{\kappa\kappa'}|\boldsymbol{q}) u_\beta(\boldsymbol{q}, \boldsymbol{\kappa'}) = \omega^2 u_\alpha(\boldsymbol{q}, \boldsymbol{\kappa}), \tag{2.17}$$

where $D_{\alpha\beta}(\boldsymbol{\kappa\kappa'}|\boldsymbol{q})$ is called as dynamical matrix and it is written as,

$$D_{\alpha\beta}(\boldsymbol{\kappa\kappa'}|\boldsymbol{q}) = \frac{1}{\sqrt{m_\kappa m'_\kappa}} \sum_{\boldsymbol{l'}\beta} \Phi_{\alpha\beta}(\boldsymbol{0\kappa}, \boldsymbol{l'\kappa'}) \exp\left[-i\boldsymbol{q}\cdot(\boldsymbol{r}(\boldsymbol{0\kappa}) - \boldsymbol{r}(\boldsymbol{l'\kappa'}))\right]. \tag{2.18}$$

Eq.(2.17) is the eigenvalue problem for $3m \times 3m$ dynamical matrix $\boldsymbol{D}(\boldsymbol{q})$. By solving this eigenvalue problem, we get $3m$ eigenvalues $\omega^2(\boldsymbol{q}, \nu)$, which are squared phonon frequencies, and eigenvectors $\boldsymbol{\lambda}(\boldsymbol{q}, \nu)$ as,

$$\boldsymbol{D}(\boldsymbol{q})\boldsymbol{\lambda}(\boldsymbol{q}, \nu) = \omega^2(\boldsymbol{q}, \nu)\boldsymbol{\lambda}(\boldsymbol{q}, \nu) \qquad (\nu = 1, 2, \cdots, 3m), \tag{2.19}$$

where eigenvectors are normalized as,

$$|\boldsymbol{\lambda}(\boldsymbol{q}, \nu)| = 1. \tag{2.20}$$

The crystal structure is dynamically stable if its potential energy always increases against any combinations of small atomic displacements. In the harmonic approximation, this is equivalent to the condition that all squared phonon frequencies $\omega^2(\boldsymbol{q}, \nu)$ are positive. On the other hand, some negative squared frequencies, which lead imaginary frequencies, appear from the eigenvalue problem under some conditions. The phonon modes which have these imaginary phonon frequencies are called imaginary phonon modes. Imaginary phonon modes indicate dynamical instability, which means the collective atomic displacements are expected to reduce the potential energy from the given equilibrium atomic positions, where the eigenvectors $\boldsymbol{\lambda}(\boldsymbol{q}, \nu)$ provide the direction of this atomic displacements [26]. Imaginary phonon modes are well recognized to provide useful information to study displacive phase transition [20, 42].

2.4 Computational Details

Table 2.1: Crystal optimization parameters for HCP crystal structures

	Cutoff Energy [eV]	Smearing Width [eV]	Sampling Mesh
Mg	525	0.5	$17 \times 17 \times 10$
Ti	400	0.3	$15 \times 15 \times 8$

For first-principles calculations, we employed the plane-wave basis projector augmented wave method (PAW) [43] within the framework of density functional theory (DFT) as implemented in Vienna *ab initio* simulation package (VASP) [22–25] and the generalized gradient approximation (GGA) of the Perdew-Burke-Ernzerhof (PBE) form [44] was used as the exchange correlation potential. The 2p and 3s electrons for Mg and the 3p, 3d and 4s elections for Ti were treated as valence and the remaining elections were kept frozen. The optimization parameters for HCP crystal structures are shown in Table 2.1. The plane-wave cutoff energy and smearing width of the Methfessel-Paxton scheme [45] shown in Table 2.1 were also used in first-principles phonon calculations. In general, the use of denser k-point sampling mesh provides better calculation accuracy at a constant smearing width and necessitates higher computational demands. On the other hand, a larger smearing width value sacrifices the detail of electronic structure, but makes it faster to converge the electronic self-consistent field iteration process. In order to make the balance between the computational cost and its accuracy, structure optimization parameters were carefully evaluated. After optimization, $\{10\bar{1}2\}$ CTB structures were constructed, which contain forty-four atoms in the unit cell as described in Section 2.2. Crystal structure optimization calculations were also conducted for $\{10\bar{1}2\}$ CTB structures. During the optimization calculations for $\{10\bar{1}2\}$ CTB

structures, atomic positions were optimized under the fixed lattice condition in order to make the analyses easier. The k-points mesh is selected as $14\times8\times1$ and is shifted by a half grid distance along a^* and b^* axis directions from the Γ centered mesh. The structure optimizations were performed until forces acting on atoms converge to less than 3×10^{-5}eV / Å.

For first-principles phonon calculations, we employed finite displacement method [46] implemented in phonopy software package [26]. For extracting Hellmann-Feynman forces from first-principles calculations, $4 \times 4 \times 3$ and $3 \times 1 \times 1$ supercells were used for HCP crystal structures and $\{10\bar{1}2\}$ CTB structures, respectively, and added 0.01 Å of atomic displacements. To obtain atomic forces, total energies were minimized until the energy convergences became less than 10^{-7} eV. The number of sampling mesh is selected to have equivalent density in reciprocal space with that of structure optimization. For Mg, $4 \times 4 \times 3$ and $5 \times 6 \times 1$ k-points were used for HCP and $\{10\bar{1}2\}$ CTB structures for phonon calculations. For Ti, $4 \times 4 \times 3$ and $4 \times 6 \times 1$ k-points were used for HCP and $\{10\bar{1}2\}$ CTB structures for phonon calculations.

To perform systematic calculations, we employed AiiDA environment, which provides high-throughput computer simulations [47].

2.5 Results and Discussions

2.5.1 Phonon structures of Mg and Ti $\{10\bar{1}2\}$ CTB under zero shear stress

Lattice parameters of Mg and Ti HCP structures after structure optimization a^{h} and c^{h} are shown in Table 2.2. The twinning shear of the $\{10\bar{1}2\}$ twinning mode is given as $s^{\mathrm{t}} = \frac{|3-\gamma^2|}{\sqrt{3}\gamma}$ with $\gamma = c^{\mathrm{h}}/a^{\mathrm{h}}$ [8]. These values are also represented in Table.2.2. Using relaxed HCP metals, $\{10\bar{1}2\}$ CTB structures were built and structure optimization with first-principles calculations were

conducted under the fixed lattice condition. Lattice parameters of $\{10\bar{1}2\}$ CTB structures shown in Table.2.2 can be calculated from the relation Eq.(2.3). Mg has the closer γ value to that of ideal ratio 1.633 than Ti, which results in the smaller twinning shear strain s^{t}. This indicates twin boundary migration in Mg $\{10\bar{1}2\}$ twin is expected to occur with smaller shear strain than Ti $\{10\bar{1}2\}$ twin.

Table 2.2: Lattice parameters of HCP and twin boundary structures. The twinning shear strains of the $\{10\bar{1}2\}$ twinning mode s^{t} are also shown.

	a^{h} [Å]	c^{h} [Å]	a [Å]	b [Å]	c [Å]	γ	s^{t}
Mg	3.19	5.19	3.19	7.58	41.60	1.63	0.126
Ti	2.94	4.65	2.94	6.89	37.74	1.58	0.181

Phonon band structures and phonon density of states (DOS) for HCP and $\{10\bar{1}2\}$ CTB structures in Mg and Ti are shown in Fig.2.6 and Fig.2.7. The space-group types of HCP and $\{10\bar{1}2\}$ CTB structures are $P6_3mmc$ (No. 194) and $Pmmn$ (No. 59) respectively. For detecting space-group types, spglib software [48] were used. High symmetry paths in reciprocal space were gotten from seekpath software [49]. The high symmetry points shown in the band structures are $\Gamma(0,0,0)$, $\mathrm{A}(0,0,1/2)$, $\mathrm{K}(1/3,1/3,0)$, $\mathrm{H}(1/3,1/3,1/2)$, $\mathrm{M}(1/2,0,0)$ and $\mathrm{L}(1/2,0,1/2)$ for HCP structures, and $\Gamma(0,0,0)$, $\mathrm{X}(1/2,0,0)$, $\mathrm{S}(1/2,0,1/2)$, $\mathrm{Y}(0,0,1/2)$, $\mathrm{Z}(0,1/2,0)$, $\mathrm{U}(1/2,1/2,0)$, $\mathrm{R}(1/2,1/2,1/2)$ and $\mathrm{T}(0,1/2,1/2)$ for CTB structures. Because the unit cell of the twin boundary structures have a large $\boldsymbol{c}$ basis vector, Y-Γ and U-R paths are small in reciprocal space as represented in the phonon bands in Fig.2.6 and Fig.2.7. For all phonon band structures, the imaginary phonon mode is not shown and, therefore, these structures are dynamically stable. The shapes of DOS for HCP and CTB structures in Mg are similar in that both DOS have first peaks at 4 THz and second

peaks at 7 THz. This indicates the vibrations of the atoms far from twin boundary is similar with that of the atoms in bulk and is not affected by the atomic vibrations around twin boundary. On the contrary, DOS peaks of bulk HCP and CTB in Ti are not as similar as that of Mg. This indicates the vibrations of the atoms far from twin boundary is affected by the atomic vibrations around twin boundary.

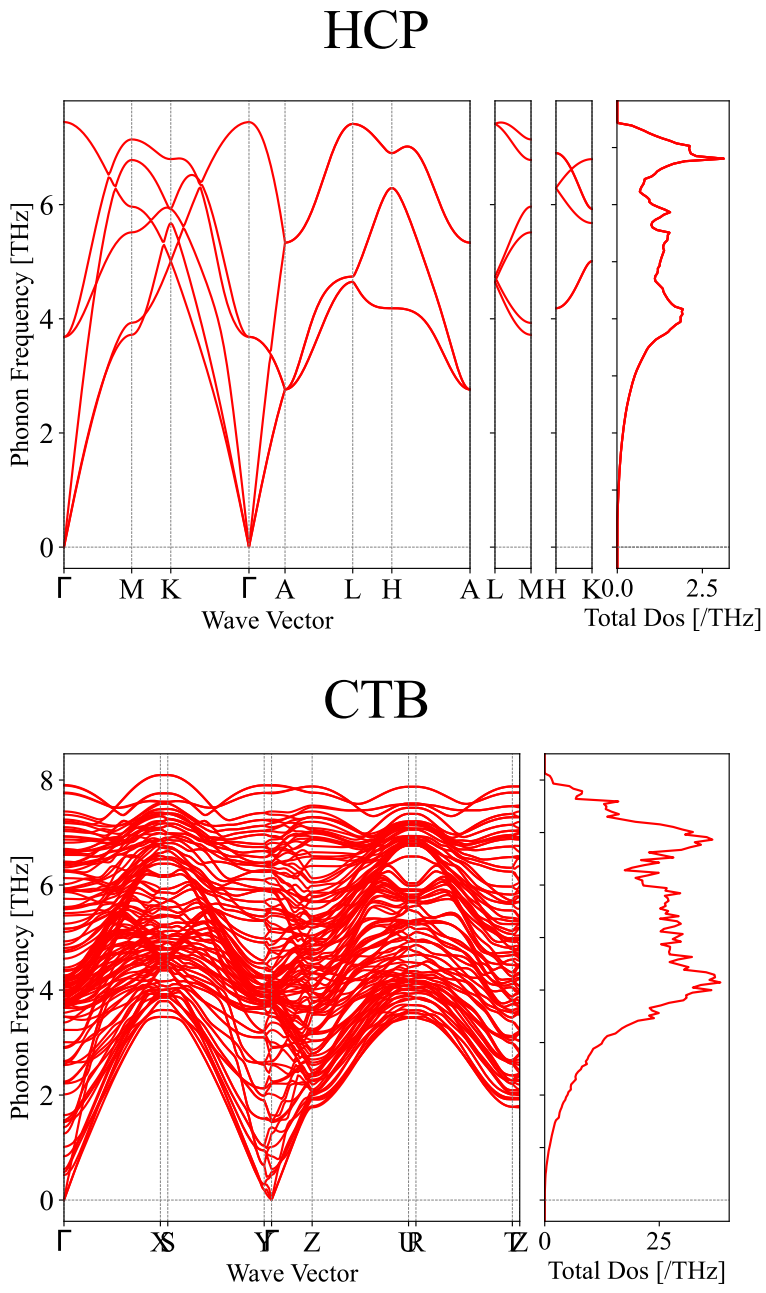

Figure 2.6: Phonon band structures and phonon DOSes of bulk HCP and CTB structures are shown in Mg. High symmetry paths in reciprocal space were gotten from seekpath software [49]. The high symmetry points shown in the band structures are $\Gamma(0,0,0)$, $A(0,0,1/2)$, $K(1/3,1/3,0)$, $H(1/3,1/3,1/2)$, $M(1/2,0,0)$ and $L(1/2,0,1/2)$ for HCP structures, and $\Gamma(0,0,0)$, $X(1/2,0,0)$, $S(1/2,0,1/2)$, $Y(0,0,1/2)$, $Z(0,1/2,0)$, $U(1/2,1/2,0)$, $R(1/2,1/2,1/2)$ and $T(0,1/2,1/2)$ for twin boundary structures.

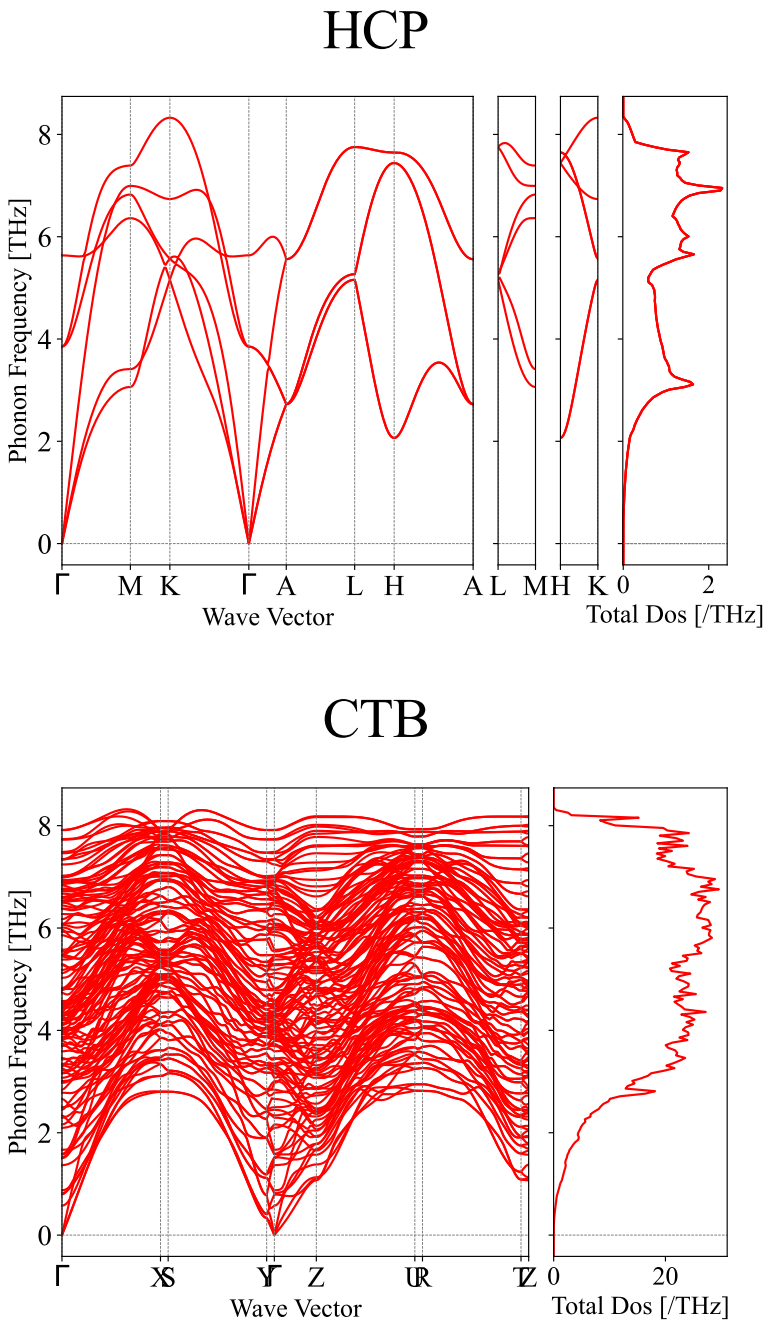

Figure 2.7: Phonon band structures and phonon DOSes of bulk HCP and CTB structures are shown in Ti. High symmetry paths in reciprocal space were gotten from seekpath software [49]. The high symmetry points shown in the band structures are $\Gamma(0,0,0)$, $A(0,0,1/2)$, $K(1/3,1/3,0)$, $H(1/3,1/3,1/2)$, $M(1/2,0,0)$ and $L(1/2,0,1/2)$ for HCP structures, and $\Gamma(0,0,0)$, $X(1/2,0,0)$, $S(1/2,0,1/2)$, $Y(0,0,1/2)$, $Z(0,1/2,0)$, $U(1/2,1/2,0)$, $R(1/2,1/2,1/2)$ and $T(0,1/2,1/2)$ for twin boundary structures.

If we don't care about the computational cost, atomic positions and their vibrations can be expected to converge to that of atoms in bulk by extending the unit cell along *c* axis. However, the computational demands become drastically expensive when we use the larger unit cell and this is almost impossible. Therefore, we need to check how atoms far from twin boundary converge to that of bulk state in the unit cell used in this work. From here, we discuss how mush atomic positions and their vibrations far from twin boundary are affected by the twin boundary and are deviated from bulk state. For simplicity, we define 1st, 2nd, 3th, 4th and 5th layer in order of closer $\{10\bar{1}2\}$ plane to the twin boundary. In Fig.2.8, the variations of $\{10\bar{1}2\}$ plane intervals in Mg and Ti $\{10\bar{1}2\}$ CTB structures before and after structure optimizations are shown. The red and the blue lines show the plane interval between $\{10\bar{1}2\}$ planes before and after crystal structure optimization. As shown with red dots in Fig.2.8, the plane intervals before crystal optimization are equivalent and they are changed by minimum potential energy searching as shown with blue dots. Both the plane intervals at the twin boundaries expanded by crystal optimization and the expansion value were 0.03 Å for Mg and 0.01 Å for Ti. For Mg, the plane intervals converge to that of bulk state as the distance from twin boundary becomes larger and the difference between the interval of bulk state and that of between 4th and 5th layers is negligible and, thus, is expected to converge to the bulk state. On the other hand, the plane intervals of Ti did not as much converge as in Mg. Therefore, it is preferable to take the larger unit cell for more accurate calculation for Ti when the computational cost is ignored.

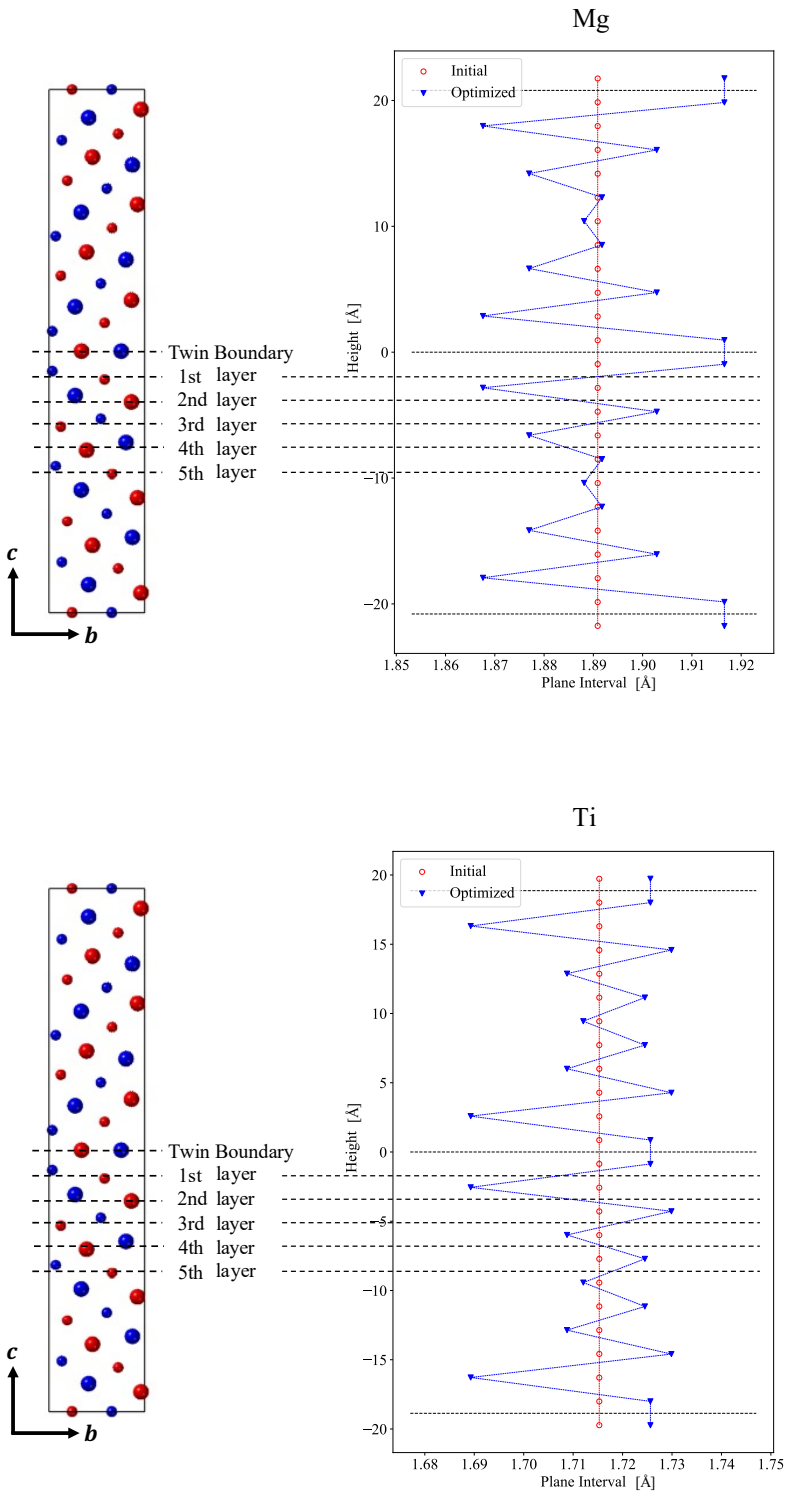

Figure 2.8: The variations of the $\{10\bar{1}2\}$ plane intervals in Mg and Ti $\{10\bar{1}2\}$ CTB structures are shown. The red and the blue lines show the plane interval between $\{10\bar{1}2\}$ planes before and after crystal structure optimization.

We also checked the convergence of atomic vibration state by decomposing total DOS into its contributions from atoms. Total DOS $g(\omega)$ is given as,

$$g(\omega) = \frac{1}{N} \sum_{\boldsymbol{q},\nu} \delta(\omega - \omega(\boldsymbol{q}, \nu)) |\boldsymbol{\lambda}(\boldsymbol{q}, \nu)|^2, \tag{2.21}$$

where $|\boldsymbol{\lambda}(\boldsymbol{q}, \nu)|^2 = 1$ and this can be decomposed into its contributions from each atom $g^\kappa(\omega)$ as,

$$g^\kappa(\omega) = \frac{1}{N} \sum_{\boldsymbol{q},\nu} \delta(\omega - \omega(\boldsymbol{q}, \nu)) |\boldsymbol{\lambda}^\kappa(\boldsymbol{q}, \nu)|^2, \tag{2.22}$$

where κ is a label of an atom in the unit cell. As denoted in Section 2.2, each $\{10\bar{1}2\}$ layer has two atoms in the unit cell. Therefore, we can get the contributions from $\{10\bar{1}2\}$ layers to total DOS by summing up the contributions from atoms on the same layer. We call this contributions from layers to total DOS as "projected DOS" throughout this section. Fig.2.9 shows the total DOS contributions from twin boundary, 2nd and 4th $\{10\bar{1}2\}$ layer. The local atomic positions are expected to converge to that of the atoms in bulk HCP in order of twin boundary, 2nd and 4th layer in order of the distance from twin boundary. Because there are two atoms on a single layer in the unit cell, the area in projected DOS is 6, which is the same as that of total DOS of bulk HCP depicted with black dotted lines in Fig.2.9. In Mg, projected DOS of twin boundary is deviated from bulk HCP total DOS. The first peak of projected DOS for twin boundary is shown at 3.5 THz where that of bulk is shown at 4 THz, and the values of density of states under the first peak for twin boundary layer become systematically bigger than that of bulk, which means the atomic vibrations at twin boundary are softer than that of bulk. On the other hand, the shape of projected DOS of 4th layer, which is far from twin boundary and denoted with the green line in Fig.2.9, agrees well with total DOS of bulk HCP, which means the vibrations of atoms on the 4th layer are converged to that of atoms in bulk.

In Ti, the first peak of projected DOS for twin boundary has also lower frequency compared with the total DOS of bulk state, where it is shown at 2.6 THz where that of bulk is shown at 3.1 THz. Therefore, the atomic vibrations at twin boundary also becomes soft in Ti. As for 4th layer in Ti denoted with green line, the shape of projected DOS did not agree with the total DOS of bulk state compared with in Mg. However, at lower frequencies under 2 THz the projected DOS of 4th layer and the total DOS of bulk state agree well, which means the atomic vibrations which have lower frequencies agree well with the bulk state.

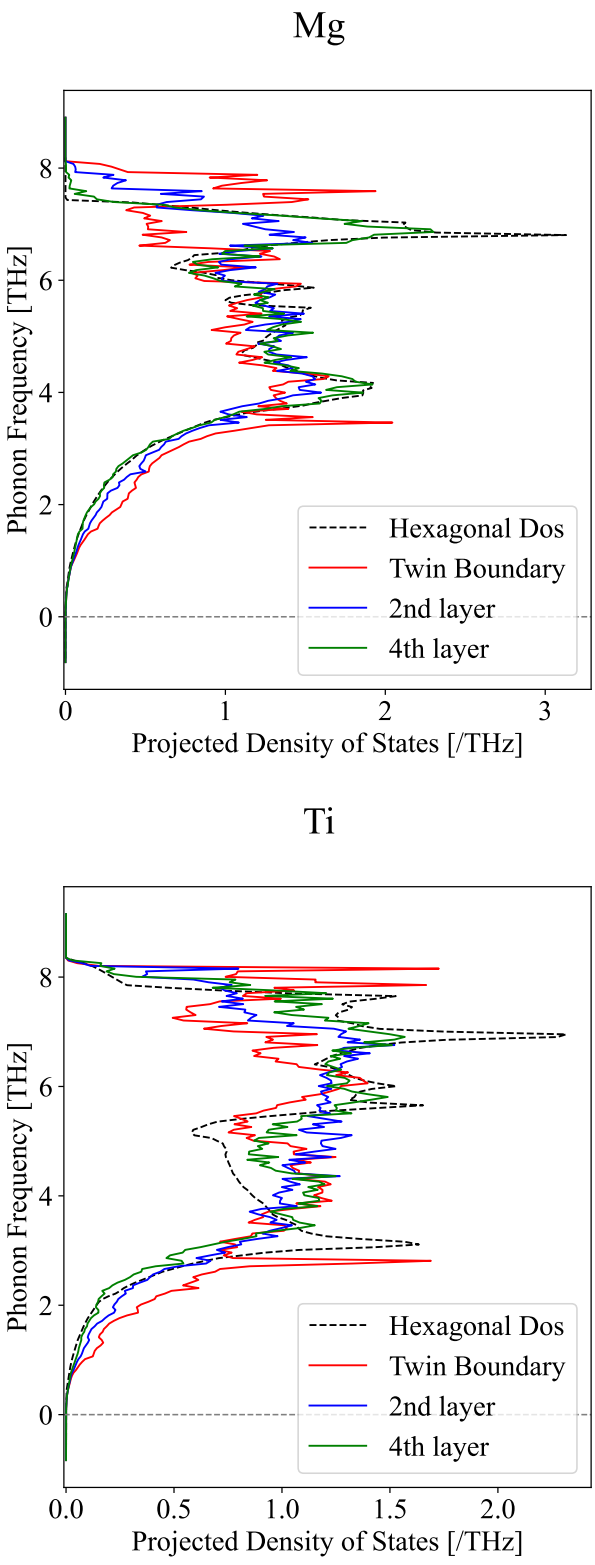

Figure 2.9: Total DOS contributions from atoms at twin boundary, 2nd and 4th $\{10\bar{1}2\}$ layer are shown in Mg and Ti $\{10\bar{1}2\}$ CTB structures. The black dotted lines represent the total DOSes of HCP structures, which indicate the bulk state.

2.5.2 Phonon structure changes of Mg and Ti CTB with external shear stress

On the purpose of revealing how the phonon structure change by adding external shear stress, shear strains were applied toward CTB structures. Let shear strain be s, sheared lattice $[\boldsymbol{a}^{\mathrm{s}}, \boldsymbol{b}^{\mathrm{s}}, \boldsymbol{c}^{\mathrm{s}}]$ is written as,

$$\begin{cases} \boldsymbol{a}^{\mathrm{s}} = \boldsymbol{a} \\ \boldsymbol{b}^{\mathrm{s}} = \boldsymbol{b} \\ \boldsymbol{c}^{\mathrm{s}} = \boldsymbol{c} + s\dfrac{|\boldsymbol{c}|}{|\boldsymbol{b}|}\boldsymbol{b}. \end{cases} \tag{2.23}$$

In this study, the structure optimizations with fixed lattice and first-principles phonon calculations were repeated while adding shear strain little by little until the imaginary phonon modes show. Shear strains $s = \{0, 0.001, 0.002, \cdots 0.01\}$ were added toward Mg CTB structure, and shear strains $s = \{0, 0.001, 0.002, \cdots 0.014\}$ were added toward Ti CTB structure, respectively. Fig.2.10(a) and Fig.2.11(a) show the changes of phonon band structures by external shear stress in Mg and Ti CTB structures. Though the phonon band structures with and without shear stress do not show much variation at higher phonon frequencies both in Mg and Ti, the frequencies of phonon modes clearly change by adding shear stress at the lower phonon frequency, especially around Γ point. As a result, the imaginary phonon modes emerged at $s = 0.01$ in Mg and at $s = 0.014$ in Ti. Fig.2.10(b) and Fig.2.11(b) are enlarged views at $\Gamma - \mathrm{X}$, $\mathrm{Y} - \Gamma$ and $\Gamma - \mathrm{Z}$ below 3 THz of phonon frequency. These high symmetry paths are along $\boldsymbol{a}^*$, $\boldsymbol{c}^*$ and $\boldsymbol{b}^*$ in reciprocal space. Both the imaginary phonon modes are shown at Γ point and come from the optical modes which have minimum phonon frequency at $s = 0$, which is shown with yellow dots in Fig.2.10(b) and Fig.2.11(b), and they show quite similar change.

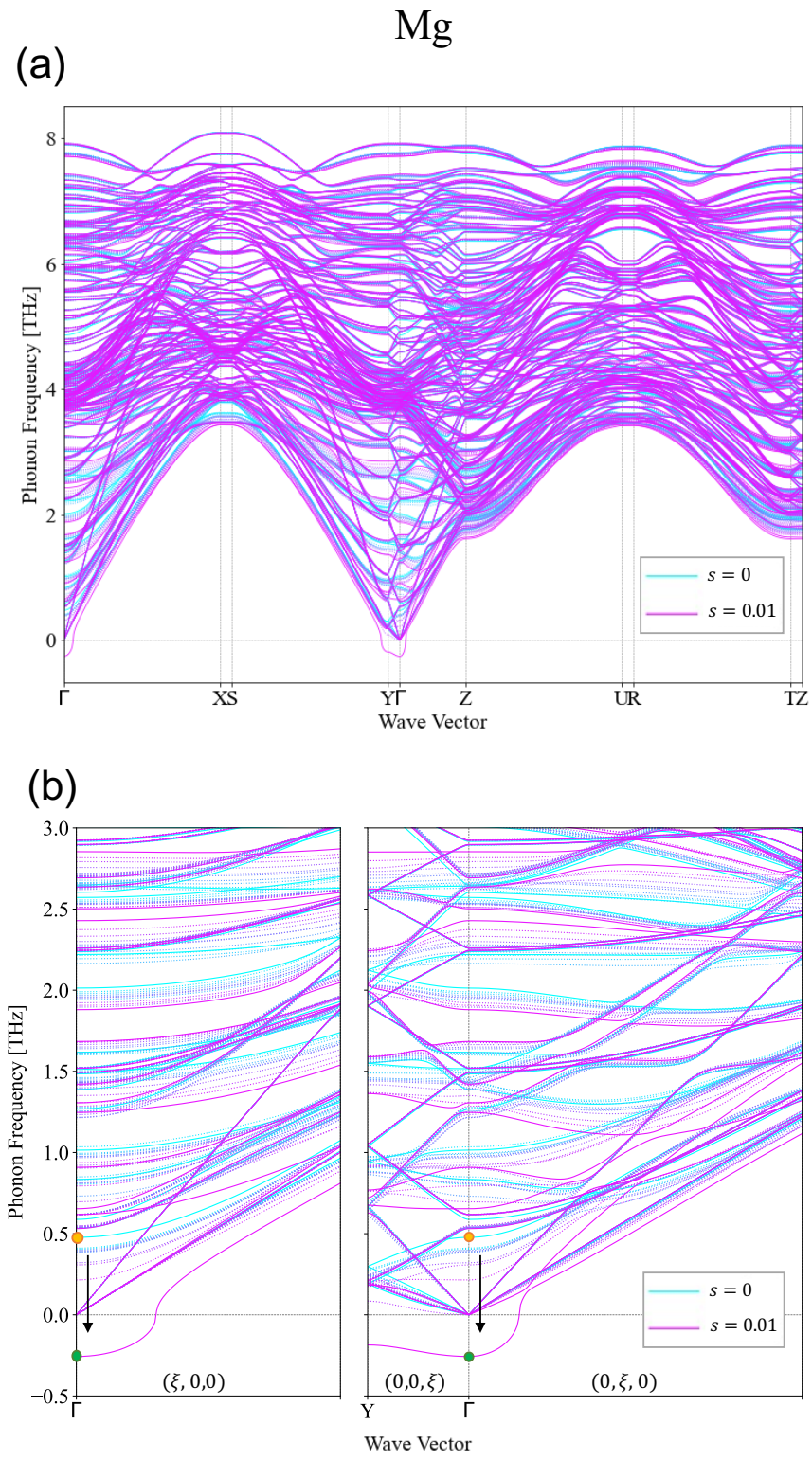

Figure 2.10: (a) Phonon band structures variation from $s = 0$ to $s = 0.01$ where the imaginary phonon mode emerge for Mg. (b) Enlarged view at Γ – X, Y – Γ and Γ – Z below 3 THz of phonon frequency. These high symmetry paths are along $\boldsymbol{a}^*$, $\boldsymbol{c}^*$ and $\boldsymbol{b}^*$ in reciprocal space.

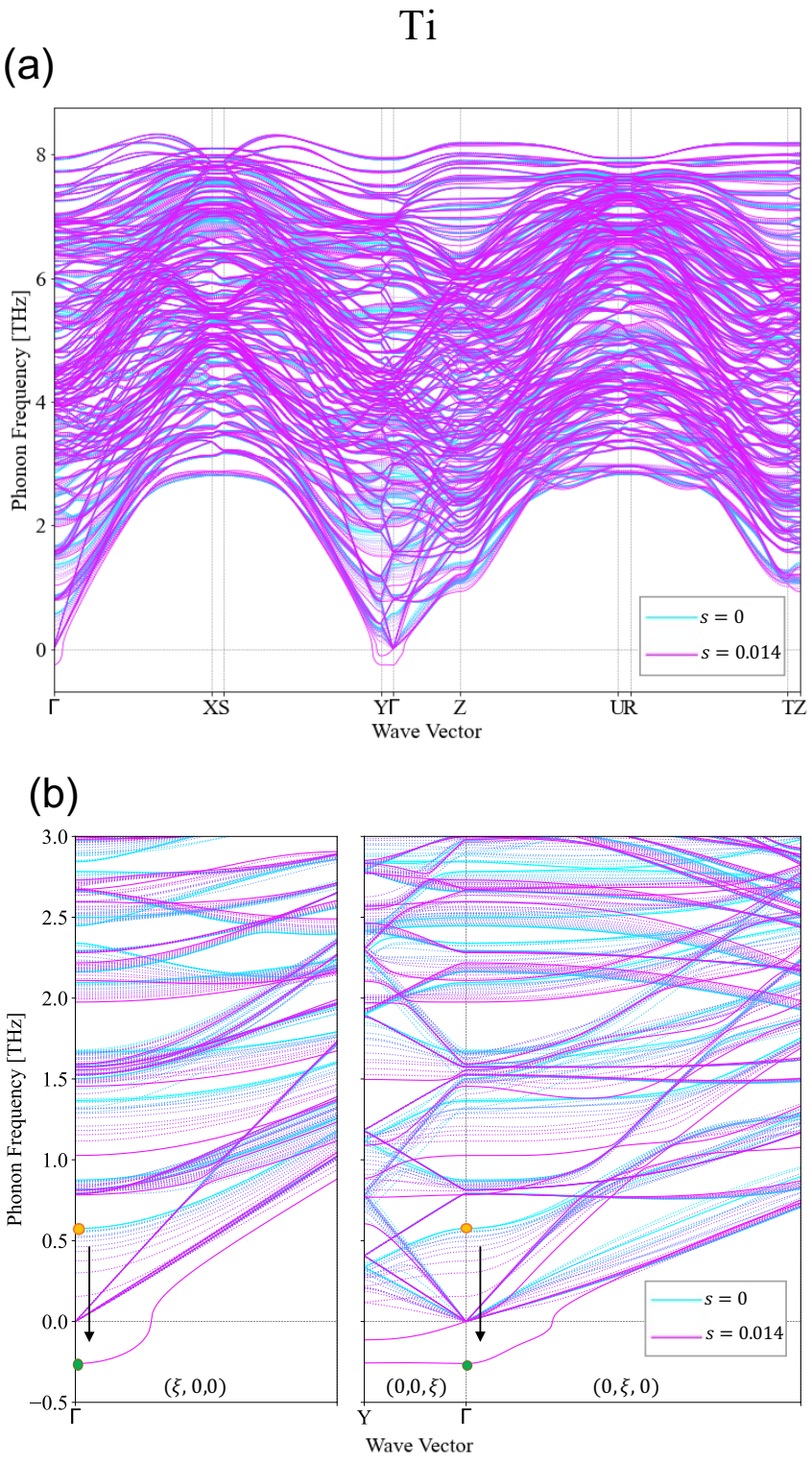

Figure 2.11: (a) Phonon band structures variation from $s = 0$ to $s = 0.014$ where the imaginary phonon mode emerge for Ti. (b) Enlarged view at Γ − X, Y − Γ and Γ − Z below 3 THz of phonon frequency. These high symmetry paths are along $\boldsymbol{a}^*$, $\boldsymbol{c}^*$ and $\boldsymbol{b}^*$ in reciprocal space.

In Fig.2.12, the atomic vibrations of the imaginary phonon modes for Mg and Ti indicated with green dots in Fig.2.10(b) and Fig.2.11(b) are shown. For visualization, the amplitudes are normalized in order that these red atoms marked with pink circle have 2 Å of the amplitudes. These two phonon modes are quite similar in that atoms around twin boundaries show rotation-like vibrations, which are indicated with yellow round arrows, where the atoms far from twin boundaries vibrate with their vibrational directions along *b* axis and the atoms in matrix have larger amplitudes than that in twin.

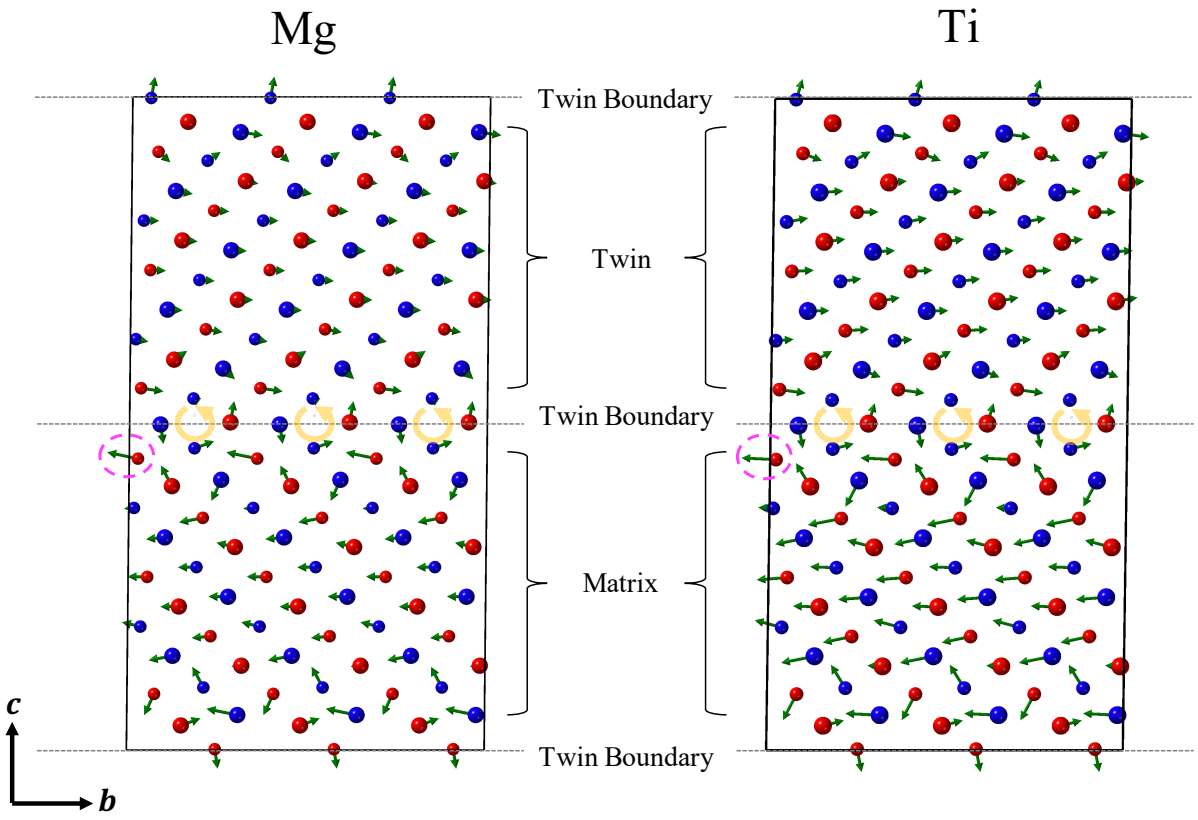

Figure 2.12: The atomic vibrations of the imaginary phonon modes for Mg and Ti indicated with green dots in Fig.2.10(b) and Fig.2.11(b) are shown. The red atoms marked with pink circle have the largest amplitudes. For visualization, the amplitudes are normalized in order that these red atoms marked with pink circle have 2 Å of the amplitudes. The atomic group rotation-like vibrations are indicated with yellow round arrows.

As described in Section 2.3, the imaginary phonon modes represent the structure is dynamically

unstable and more stable state is expected to exist along the atomic vibrational directions of the imaginary phonon modes. In order to investigate the more stable state, atomic displacements were added to the sheared structure in which the imaginary phonon modes were emerged, and the structure optimization calculations were conducted toward them both in Mg and Ti under the fixed lattice conditions. In Fig.2.13, the snapshots of Mg $\{10\bar{1}2\}$ CTB structures in each step from the initial structure to the twin boundary migrated structure. For visualization, we used common neighbor analysis (CNA) [50] implemented in OVITO software package [51]. CNA analyzes the local structure environment of each atom and categorize atoms into FCC, BCC and HCP type. The theoretical backgrounds for CNA are shown in Appendix A. In Fig.2.13, the red atoms are recognized as HCP type from the local atomic environment and the white atoms are recognized as none of FCC, BCC or HCP type. (a) is the Mg $\{10\bar{1}2\}$ CTB with zero shear and (b) is the sheared structure from (a) where the imaginary phonon mode was emerged at Γ point in reciprocal lattice. The atoms of the sheared structure (b) are displaced along the eigenvector of the imaginary phonon mode as shown in (c), where the amplitudes are normalized in order that the maximum displacement have 0.05 Å of the displace distance. (d) is the optimized structure from (c) under fixed lattice condition. During the structure optimization, the twin boundary migration was occurred as indicated with yellow arrow. The structure changes were also occurred in Ti $\{10\bar{1}2\}$ CTB structures. Therefore, from lattice dynamics point of view, the $\{10\bar{1}2\}$ CTB migrations in Mg and Ti are triggered by the phonon modes which dropped into the imaginary phonon modes at Γ point, which are indicated in Fig.2.10(b) and Fig.2.11(b), and the directions of the initial displacements of atoms for the twin boundary migrations are shown in Fig.2.12.

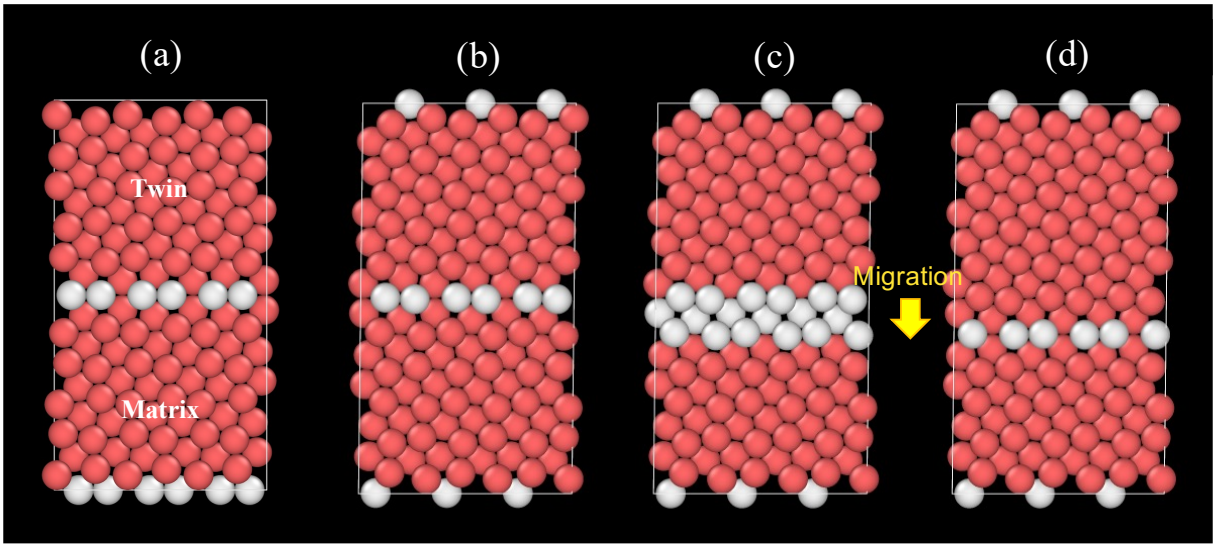

Figure 2.13: Mg $\{10\bar{1}2\}$ CTBs for each step are shown. The atomic colors are determined from CNA, where the red atoms are recognized as HCP type from the local atomic environment where and the white atoms where are recognized as neither of FCC, BCC nor HCP type. (a) is the Mg $\{10\bar{1}2\}$ CTB structure with zero shear and (b) is the sheared structure from (a) where the imaginary phonon mode were emerged. (c) is the atomic displacement added structure from (b) based on the eigenvector of the imaginary phonon mode, where the maximum displacement is 0.05 Å of the distance. (d) is the optimized structure from (c). During the structure optimization, the twin boundary migration was occurred as indicated with yellow arrow.

In Fig.2.14, the changes of the total energy and the shear stress σ_{yz} in Mg and Ti CTB structures are shown, where the dots marked with (a), (b) and (d) correspond to the (a), (b) and (d) structures represented in Fig.2.13. The red stars represent the total energies and the shear stresses of the optimized structures from the dynamically unstable structure. As shown in figures, the total energies and shear stresses increase until the imaginary phonon modes show and by optimization from dynamically unstable structures the total energies decrease and the loaded shear stresses are relieved as indicated with the yellow arrows. Therefore, the sheared CTB structures are stabilized by twin boundary migration. From these results, we can conclude that the twin boundary migrations in Mg and Ti CTB structures are occurred by the following two steps. First, the total energy is increased by external shear stress until the structure are dynamically unstable. Then, the atomic

group rotation-like rearrangement around twin boundary occurs triggered by the imaginary phonon mode and this results in the twin boundary migration.

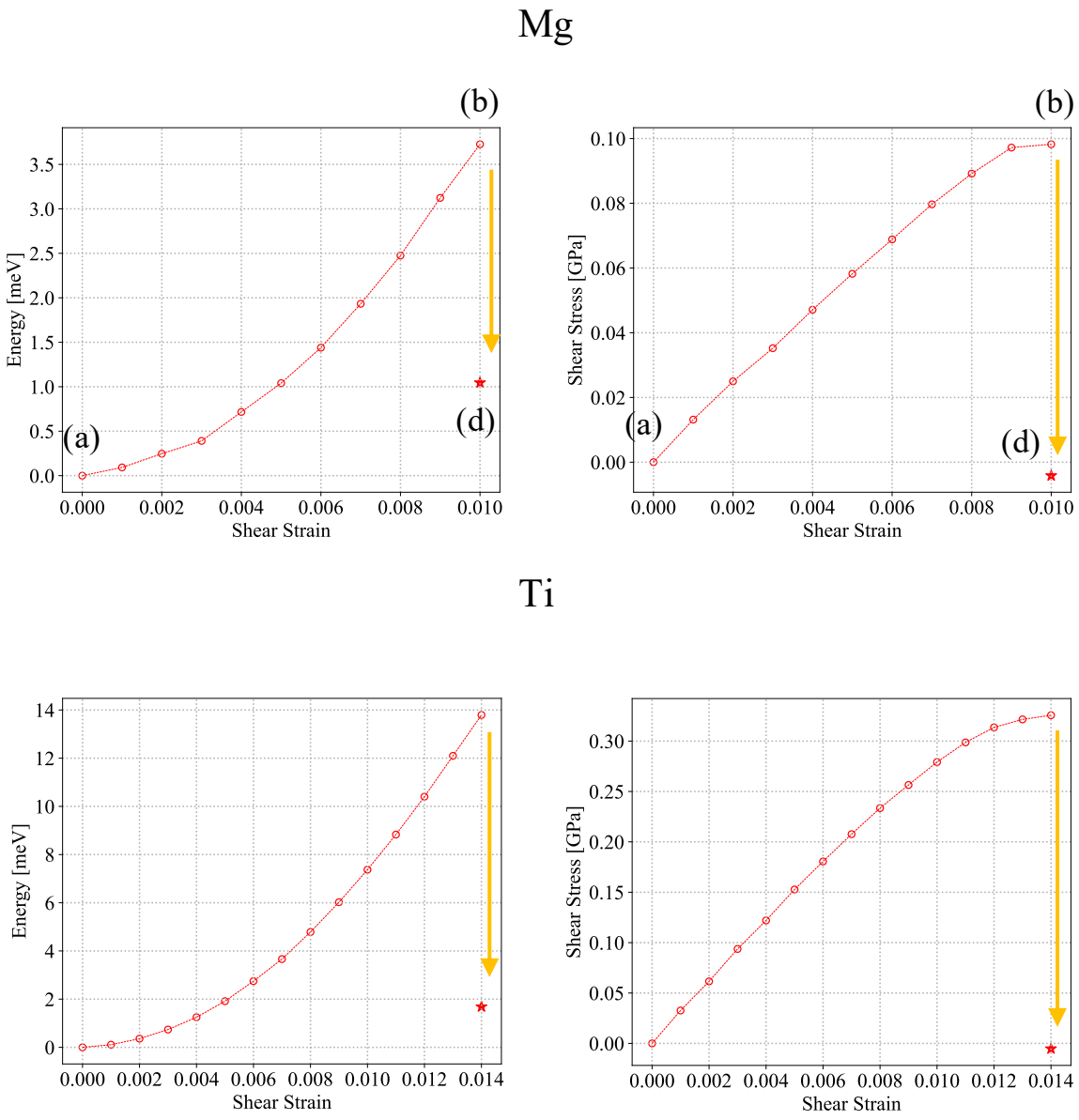

Figure 2.14: The changes of the total energy and the shear stress σ_{yz} are shown, where the dots marked with (a), (b) and (d) correspond to the (a), (b) and (d) structures represented in Fig.2.13. The red stars represent the total energies and the shear stresses of the optimized structures from the sheared and dynamically unstable structure. During optimization, the total energies are decreased and the loaded shear stresses are relieved as indicated with the yellow arrows.

2.6 Conclusion

In this chapter, we investigated the phonon structures of Mg and Ti $\{10\bar{1}2\}$ CTB with and without shear strain. Under zero shear strain condition, both twin boundaries have no imaginary phonon mode, which means both CTB structures are dynamically stable under zero shear stress. Because our purpose in this study is to extract the phonon structure around twin boundary, it is preferable that the interactions between twin boundaries are negligible. To check how much the twin boundaries interact, we used the technique of total DOS decomposition, and revealed that the vibration state at 4th layer is converged well to the bulk in Mg, but the convergence was not so better in Ti. This indicates the structure size along c axis is enough in Mg. As for Ti, if computational cost for first-principles calculations can be ignored, it is better to use larger simulation cell for calculations.

By adding shear strain to Mg and Ti CTB structures, the imaginary phonon modes were emerged at shear strain $s = 0.01$ in Mg and shear strain $s = 0.014$ in Ti at Γ point. Because the imaginary phonon modes indicate the sheared CTB structures are dynamically unstable and their eigenvectors have a clue to obtain the new dynamically stable structures, the atomic displacements based on the eigenvectors of the imaginary phonon modes were applied to the sheared CTB structures and the structure optimizations were conducted toward the displacements added structures. As a result, the twin boundary migrations were occurred both in Mg and Ti accompanied with atomic rotation-like rearrangement around twin boundaries. During optimizations, the total energies were decreased and the loaded shear stresses were relieved. Therefore, the sheared CTB structures are stabilized by twin boundary migrations. From these results, we can conclude that the twin boundary migrations in Mg and Ti CTB structures are occurred by the following two steps. First, the total energy is increased by external shear stress until the structure are dynamically unstable. Then, the atomic

group rotation-like rearrangement around twin boundary occurs triggered by the imaginary phonon mode and this results in the twin boundary migration.

From these results, we can conclude the phonon structure analysis is useful for the study of the twin growth in CTB structures because the atomic path during the twin boundary migration is characterized by the imaginary phonon modes and give us the answer for the basic question, "how atoms move during twin growth", from atomic and dynamic point of view.

Chapter 3

Atomic Mechanism of Twin Growth of Dual Step Introduced $\{10\bar{1}2\}$ Twin Boundaries in Mg and Ti

3.1 Introduction

In Chapter 2, we revealed the atomic scale twin growth mechanism in Mg and Ti $\{10\bar{1}2\}$ CTB structures by investigating the phonon structure changes around twin boundaries. However, as mentioned in Chapter 1, $\{10\bar{1}2\}$ twin boundary is actually not fully coherent but often deviates from theoretical one by exhibiting steps [17]. Therefore, we need to consider more actual situations in the next step. Recently, He *et al.* has succeeded to conduct an in-situ atomic scale observation of Re $\{10\bar{1}2\}$ twin growth, where they found out the migration of twin boundary is proceeded by the dual steps sweeping on the twin boundary during detwinning process [19]. The dual steps meditated twin growth mechanism has been already proposed by Pond, Hirth, Serra and Bacon. They considered the twin boundary migration is meditated by the steps formed at the interface and introduced the concept

"disconnection", which is interfacial defect exhibiting both dislocation and step character [11, 12]. In FIG.3.1, the disconnection introduced Mg $\{10\bar{1}2\}$ twin boundary model is shown [37, 52]. Ostapovets *et al.* report in their paper that twin boundary migrates by the disconnection gliding along the twin boundary during molecular dynamics (MD) simulation [52]. The concept of disconnection is useful to describe the topology of the step introduced twin boundaries and it has become widely used in study of twin nucleation and growth [53–58].

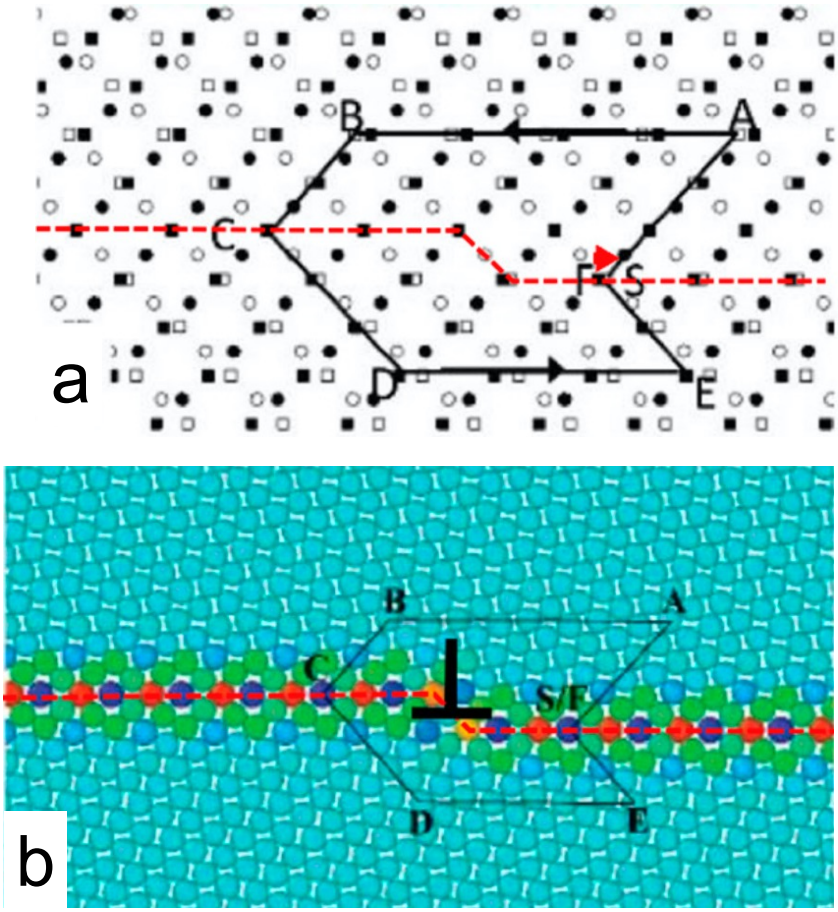

Figure 3.1: (a) Dichromatic pattern for Mg $\{10\bar{1}2\}$ twin boundary. White and black dots represent parent and twin lattice respectively. The $\{10\bar{1}2\}$ twin boundary is indicated by red dashed line and the disconnection produces step in the boundary. The burgers vector for disconnection is defined by burgers circuit indicated by black line. (b) Dichromatic complex is shown which embed atoms to each lattice point toward each lattice point in (a) [37].

Disconnection model proposes that the newly introduced disconnection sweeps along the twin boundary by external shear stress and this results in twin thickening. However, it does not say anything about what is the driving force for disconnection gliding and the atomic trajectories during twin growth based on energetic point of view, though the trajectories of some specific atoms around twin boundary during MD simulation are investigated in some papers [37, 59, 60].

In this chapter, we will reveal how the rearrangement of the atoms around $\{10\bar{1}2\}$ twin boundary, especially around the dual step which is called disconnection, occurs in Mg and Ti using a series of phonon calculations. In the following, we use the term "disconnection" for simplicity. We first describe the methods of building disconnection introduced $\{10\bar{1}2\}$ structures in Section 3.2. Because plane wave basis set is used for phonon calculations, the simulation cell must be periodic in all directions. A single disconnection introduced twin boundary cannot fulfill this restriction. Therefore, to fulfill this condition, we introduce disconnection dipole instead of a single disconnection to the $\{10\bar{1}2\}$ CTB structures following MacKain *et al*'s work [55]. The disconnection dipole introduced $\{10\bar{1}2\}$ twin boundary structures built in Section 3.2 have more than one thousand of atoms in the unit cell, which are difficult to conduct first-principles phonon calculations because of their computational cost. Therefore, we employed machine learning interatomic potentials (MLIP) developed by Seko *et al* [61, 62] for all phonon calculations in this chapter. The adopted MLIP use polynomial-based potential energy models and group-theoretical invariants for extracting structure features. The potential energy models were fitted to huge amount of DFT calculations in their work. The theoretical backgrounds of the adopted MLIP are reviewed in Section 3.3. In Section 3.4, computational details for calculations are described. We also check the accuracy of phonon calculations with MLIP by comparing the results with first-principles phonon calculations in this section. In Section 3.5, the changes of phonon structures of disconnection dipole introduced $\{10\bar{1}2\}$ structures by shear strains in Mg and Ti are shown. Finally, from the imaginary phonon mode analyses, we

provide the atomic rearrangement associated with disconnection sweeping on the twin boundaries.

3.2 Modeling disconnection introduced $\{10\bar{1}2\}$ twin boundary

In this section, the method of building disconnection introduced $\{10\bar{1}2\}$ twin boundary is described. Because the demand for doing phonon calculations toward simulation cells, the simulation cells must be satisfy periodic boundary conditions in all directions, which are not fulfilled when a single disconnection is introduced. Therefore, we introduced disconnection dipole of length l instead of a single disconnection based on MacKain *et al*'s work [55].

In Fig.3.2(a), the dichromatic pattern [21, 36] is depicted where white and black dots represent hexagonal lattice points of matrix and twin lattices respectively and they are interpenetrated each other. The $\{10\bar{1}2\}$ twin boundary with disconnection dipole is determined as represented with red dashed line in Fig.3.2(a). The disconnection produces two-layer step in the boundary. Then, the burgers circuits are reproduced on the dichromatic pattern as indicated with blue dotted line. It starts from S point, runs over the black points above the twin boundary and the white points below the twin boundary, and stops at the F point. The burgers vectors for disconnection dipoles $\boldsymbol{b}_{\mathrm{D}}$ and $-\boldsymbol{b}_{\mathrm{D}}$ are defined from the mismatch between S points and F points. The absolute value b_{D} of $\pm\boldsymbol{b}_{\mathrm{D}}$ is,

$$b_{\mathrm{D}} = |\pm\boldsymbol{b}_{\mathrm{D}}| = 2ds^{\mathrm{t}}, \tag{3.1}$$

where d is the plane interval of $\{10\bar{1}2\}$ planes and s^{t} is twin shear strain value as shown in Fig.3.2(b). The simulation box of the length L along y axis and the height H along z axis is represented with black dashed line which is periodic in all directions. Let the number of replication of CTB unit cell, which is represented with black dotted line in Fig.3.2(a), along y axis be n_y and the number of $\{10\bar{1}2\}$ plane in the simulation box be n_z, the length L and the height H of the simulation box are

represented as,

$$L = n_y b, \tag{3.2}$$

$$H = n_z d, \tag{3.3}$$

where b is the length of the unit cell of CTB structure used in Chapter 2.

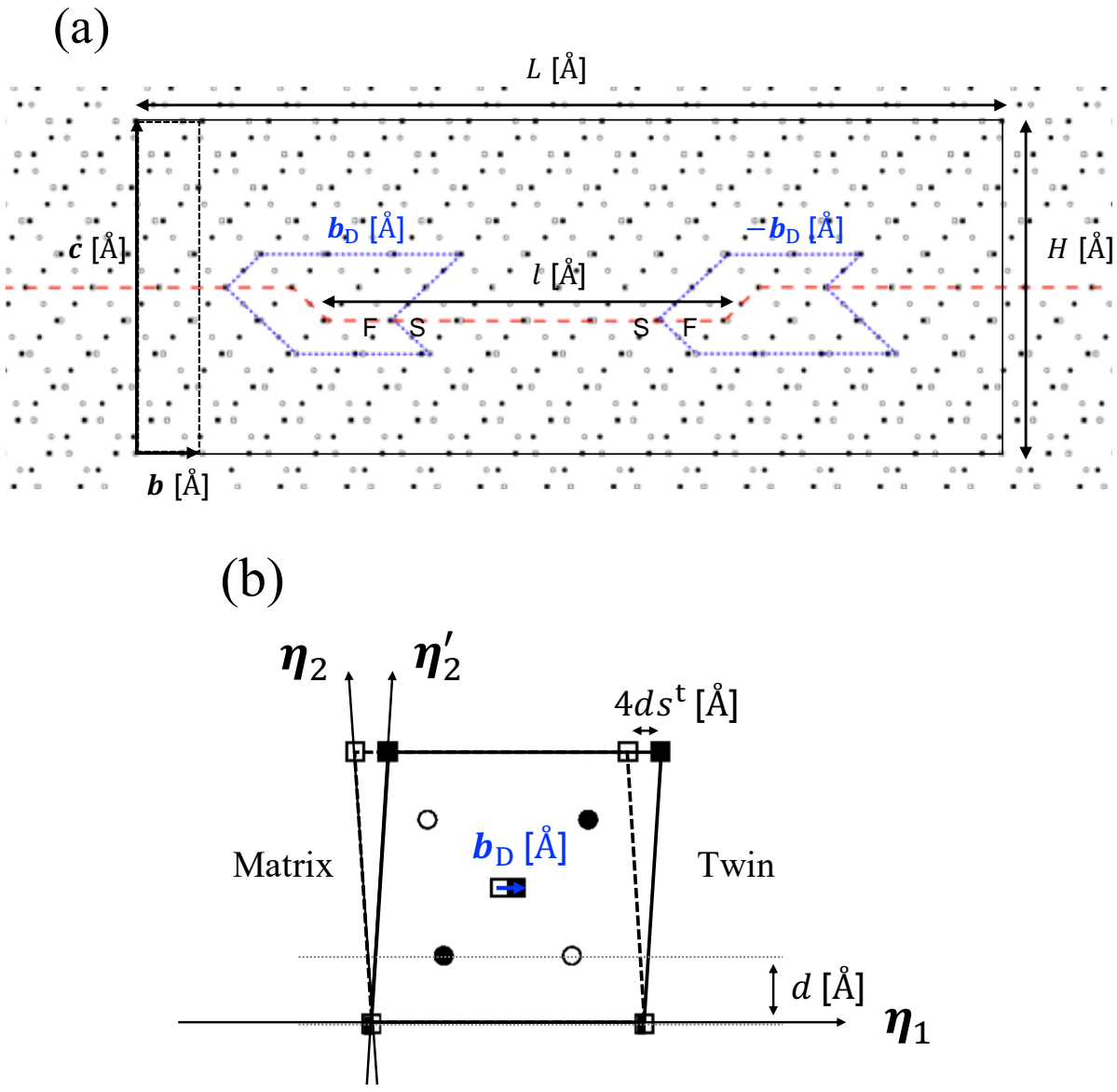

Figure 3.2: (a) The dichromatic pattern for $\{10\bar{1}2\}$ twinning mode is shown. The white and the black dots represent hexagonal lattice points of matrix and twin lattices respectively and they are interpenetrated each other. The $\{10\bar{1}2\}$ twin boundary with disconnection dipole is denoted with the red dashed line. The burgers circuits for disconnections are shown with the blue dotted lines and they determine burgers vectors $\boldsymbol{b}_{\mathrm{D}}$ and $-\boldsymbol{b}_{\mathrm{D}}$. (b) The topological relation between the burgers vector $\boldsymbol{b}_{\mathrm{D}}$ and shear strain for $\{10\bar{1}2\}$ twinning mode s^{t}. The absolute value for burgers vector $\boldsymbol{b}_{\mathrm{D}}$ is easily determined as $|\boldsymbol{b}_{\mathrm{D}}| = 2ds^{\mathrm{t}}$.

The simulation unit cell is defined by embedding atom pairs on each lattice point and get rid of atoms generated from the matrix lattice points above the boundary and atoms generated from the twin lattice points below the boundary. For the lattice points on the twin boundary, embedded atom pairs are projected onto the twin boundary. The resultant simulation unit cell is shown in Fig.3.3. Note that in addition to disconnection dipole introduced $\{10\bar{1}2\}$ twin boundary, coherent twin boundary is created at the top and the bottom, and the periodic boundary conditions are fulfilled in all directions.

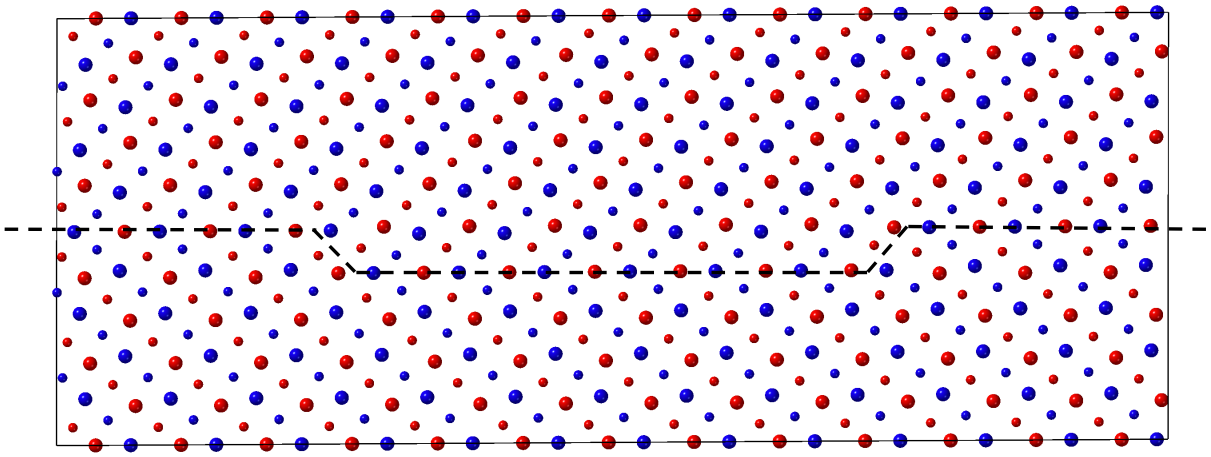

Figure 3.3: The resultant unit cell by embedding HCP atom pairs toward each lattice point in dichromatic lattice in Fig.3.2(a). The black dotted line at the middle represents disconnection dipole introduced $\{10\bar{1}2\}$ twin boundary. Matrix and twin are below and above the twin boundary, respectively. The atom pair of HCP structure is represented with red and blue spheres.

As shown in Fig.3.3, twin domain becomes larger than matrix domain by disconnection dipole. Therefore, we added the initial shear strain s^0 to the simulation unit cell to relieve the corresponding macroscopic strain, where the initial shear strain s^0 is given as [55],

$$s^0 = \frac{b_{\mathrm{D}} l}{HL}. \tag{3.4}$$

In this study, we defined $l = L/2$, $H = n_z d$ and $L = n_y b$. Using the relation Eq.(3.1), we finally get

$$s^0 = \frac{s^{\mathrm{t}}}{n_z}. \tag{3.5}$$

In this study, we selected three different size simulation cells to check the convergence, where the parameters of these three simulation cells are $n_z = 22$ and $n_y = \{29, 39, 49\}$.

3.3 Machine learning interatomic potential based on high-order rotational invariants

In this section, we review machine learning interatomic potential (MLIP) from group theoretical high-order linearly independent rotational invariants from structural representations [61].

The MLIP is based on the idea that the total energy of a system E can be decomposed into the contributions of each atom in the system $E^{(i)}$, which we call as atomic energy throughout this section, as,

$$E = \sum_i E^{(i)}. \tag{3.6}$$

If we consider the atomic energy $E^{(i)}$ is determined by the interactions between the atoms surrounding the specific atom i, the atomic energy $E^{(i)}$ becomes functional of the atomic density $\rho^{(i)}$ as,

$$E^{(i)} = \mathcal{F}[\rho^{(i)}]. \tag{3.7}$$

If cutoff radius r_c is given where the atoms within the cutoff radius interact with atom i, the atomic

density can be written as the summation of delta functions,

$$\rho^{(i)} = \sum_j \delta(\boldsymbol{r} - \boldsymbol{r}^{(j)}) \qquad (|\boldsymbol{r}^{(i)} - \boldsymbol{r}^{(j)}| < r_c), \tag{3.8}$$

where $\boldsymbol{r}^{(i)}$ and $\boldsymbol{r}^{(j)}$ are the atomic positions of atom i and atom j. By expanding the atomic density $\rho^{(i)}$ into spherical harmonics, we get,

$$\rho^{(i)}(r, \theta, \phi) = \sum_{nlm} a^{(i)}_{nlm} f_n(r) Y_{lm}(\theta, \phi), \tag{3.9}$$

where $a^{(i)}_{nlm}$ is order parameter, and $\{f_n\}$ and $\{Y_{lm}\}$ are the set of radial functions and spherical harmonics, respectively. There is an arbitrary choice as a set of radial functions and in the group theoretical model the Gaussian-type radial functions are adopted as,

$$f_n(r) = \exp[-\beta_n (r - r_n)^2] f_c(r), \tag{3.10}$$

where β_n and r_n are parameters. The cutoff function f_c is given as,

$$f_c(r) = \begin{cases} \frac{1}{2}[\cos(\pi \frac{r}{r_c}) + 1] & (r \leq r_c) \\ 0 & (r > r_c). \end{cases} \tag{3.11}$$

Let the atomic energy $E^{(i)}$ be represented as a function of a set of the structure descriptors $\{d^{(i)}_n\}$, which is called as the structure features, derived from order parameters $\{a^{(i)}_{nlm}\}$,

$$E^{(i)} = F(d^{(i)}_1, d^{(i)}_2, \cdots). \tag{3.12}$$

We have to care about the fact that although an arbitrary rotation and inversion operation generally

changes the atomic density $\rho^{(i)}$, it does not change the atomic energy $E^{(i)}$. This means the atomic energy is invariant under all the elements of SO(3) group. To fulfill this requirement, linearly independent polynomial invariants of SO(3) group generated from order parameters $a^{(i)}_{nlm}$ are adopted as structure features for the atomic energy. A pth order polynomial invariant is expressed as,

$$d^{(i)}_{nl_1l_2l_p,(s)} = \sum_{m_1,m_2,\cdots,m_p} c^{l_1l_2\cdots l_p,(s)}_{m_1m_2\cdots m_p} a^{(i)}_{nl_1m_1} a^{(i)}_{nl_2m_2} \cdots a^{(i)}_{nl_pm_p}, \tag{3.13}$$

where a coefficient set $\{c^{l_1l_2\cdots l_p,(s)}_{m_1m_2\cdots m_p}\}$ is determined by using a group-theoretical projection operator method [63].

3.4 Computational details

For the structure optimization and phonon calculation of $\{10\bar{1}2\}$ twin boundary with disconnection dipole, first-principles calculations are computationally too expensive due to their large simulation cells. On the other hand, empirical potentials are lack of accuracy for computing lattice dynamics because the differential of potential energy is needed for computing second order force constants. From these backgrounds, we selected to use MLIP from group theoretical high-order linearly independent rotational invariants from structure representations [61]. Theoretical backgrounds are shown in Section 3.3. Throughout this chapter, atomic scale simulations are performed within a molecular statics framework in LAMMPS software employing energy-minimization routines [64].

The MLIPs for a variety of elements including Mg and Ti are open to the public in Machine Learning Potential Repository [62]. The MLIPs in the repository are generated by fitting energies and forces from the DFT calculations for over thousands of structures to various kinds of model function by Lasso regression. The repository uses two sets of structure generators. One is composed

of FCC, BCC, HCP, SC, ω, and β-tin structures, which we call "COMMON" datasets in this section. The other is composed of prototype structures reported in the Inorganic Crystal Structure Database (ICSD) [65]. From these structure generators, new structures are constructed by operating random lattice expansion, lattice distortion, and random atomic displacements into a supercell of the structure generators. The accuracy and computational efficiency of the MLIPs depend on the input parameters such as the type of potential energy model and the cutoff radius. The trade-offs between the accuracy and computational efficiency are clearly represented by Pareto optimal [66]. The MLIP repository provides Pareto optimal points for every system and dataset. In Fig.3.4, Pareto optimal points for Mg and Ti extracted from the MLIP repository are shown, where RMSE represents the errors of the crystal structure energies calculated from selected MLIP toward that of DFT calculations. For Mg, the MLIPs from COMMON dataset have better accuracy than that from ICSD dataset in small elapsed time, but in the MLIPs which need higher computational cost they have almost the same accuracy. On the other hand, the MLIPs from COMMON dataset systematically have higher accuracy than that of ICSD dataset in Ti.

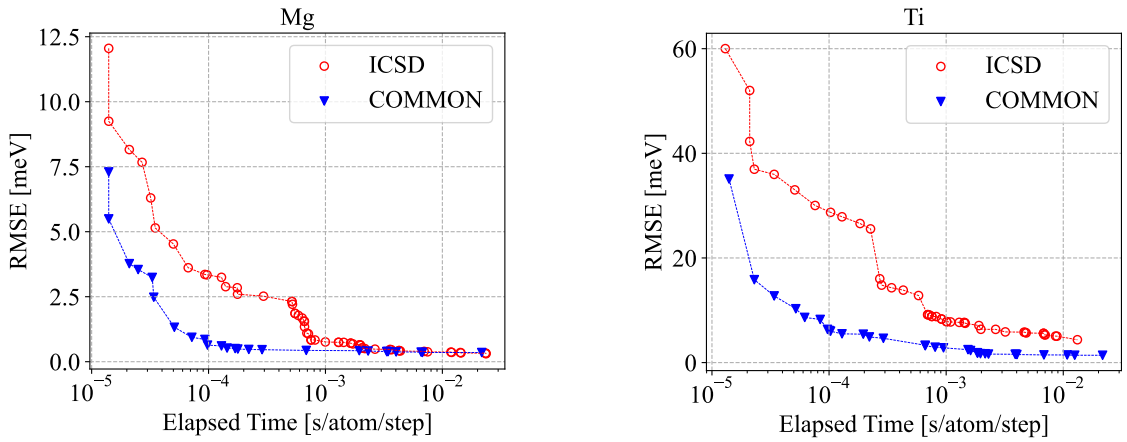

Figure 3.4: The Pareto optimal points for Mg and Ti extracted from MLIP repository are shown. Each point represents MLIP given from specific parameters. Elapsed time means a single step calculation time with selected MLIP per atom with a single CPU core and RMSE represents the errors of the crystal structure energies calculated from selected MLIP toward that of DFT. The red and blue dots represent the MLIPs generated from ICSD and COMMON datasets.

Because our purpose is to unravel the atomic dynamics around twin boundary, we need to check the accuracy of phonon calculations with MLIP in addition to the accuracy of crystal structure energy, and select appropriate MLIP. Therefore, we conducted systematic phonon calculations for HCP crystal structures and $\{10\bar{1}2\}$ twin boundaries using the Pareto optimal MLIPs and compared them with that of DFT phonon calculations. Fig.3.5 shows the RMSE of phonon frequencies from phonon calculations with MLIPs toward that from DFT calculations. The selected parameters for phonon calculations are the same as that denoted in the previous chapter. For Mg, the MLIPs generated from ICSD dataset showed better accuracy at higher computational cost potentials and the RMSE were less than 0.05 THz. The RMSE for Ti are not as small as that of Mg and the MLIPs generated from COMMON dataset showed better accuracy, which is the same trends as the RMSE for crystal structure energies shown in Fig.3.4.

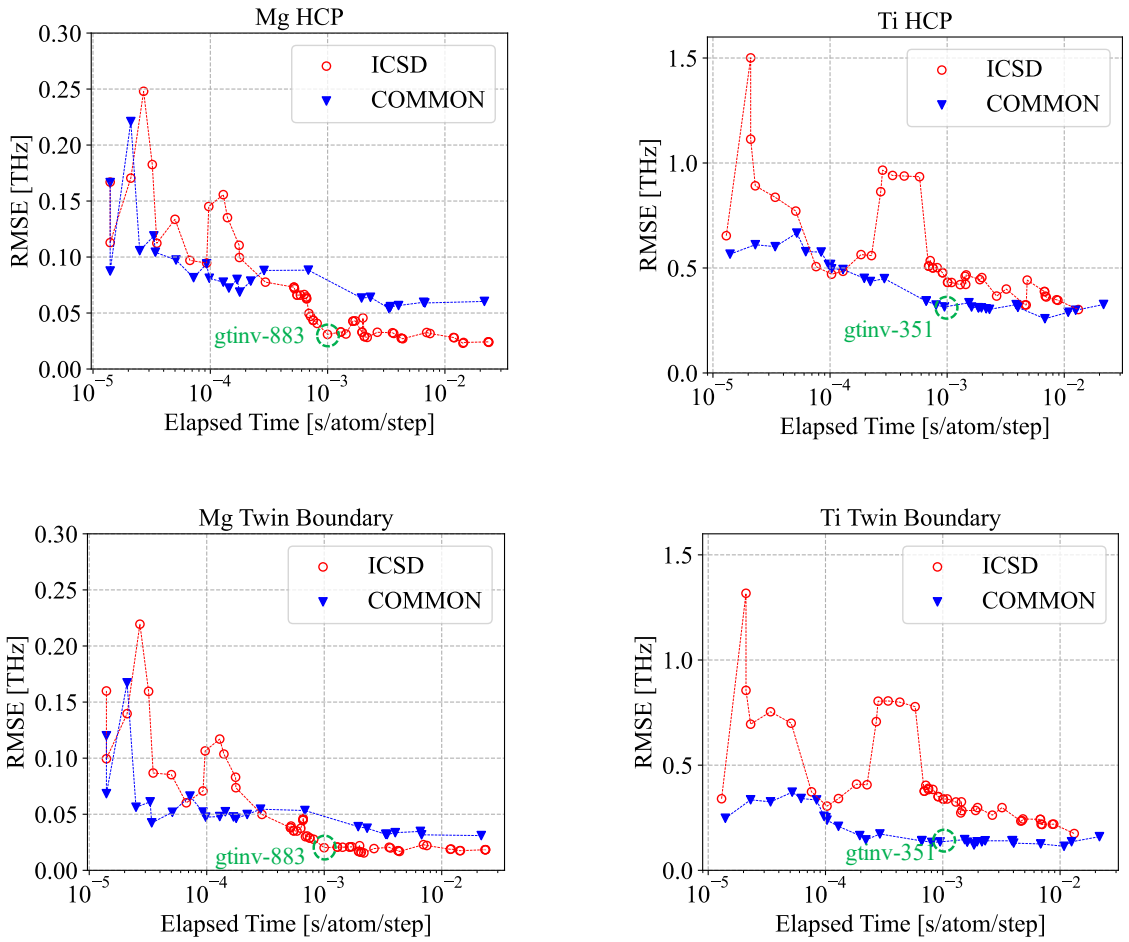

Figure 3.5: The RMSE of phonon frequencies from phonon calculations with MLIPs toward that from DFT calculations. The green dashed circle represents the MLIPs for Mg and Ti selected in this study. The label COMMON is the MLIPs which are the potentials fitted to DFT calculations toward FCC, BCC, HCP, SC, ω and β-tin structures. The label ICSD is the MLIPs are the potentials fitted to DFT calculations toward prototype structures reported in ICSD database.

From the results of phonon calculations, we selected gtinv-883 potential generated from ISCD dataset for Mg and gtinv-351 potential generated from COMMON dataset for Ti, respectively, where these potential names are used in the MLIP repository. The elapsed times of the two potentials are about 10^{-3} s/atom/step, and, therefore they need almost the same running time. Both potentials use

6 Å of cutoff radius, and the 4th and 3rd order polynomials are included for Mg and Ti, respectively. An atomic energy model is,

$$E^{(i)} = F_1(D^{(i)}) + F_2(D_1^{(i)}) + F_3(D_1^{(i)}) + \cdots , \tag{3.14}$$

for Mg gtinv-883 potential and,

$$E^{(i)} = F_1(D^{(i)}) + F_2(D_1^{(i)} \cup D_2^{(i)}) + \cdots , \tag{3.15}$$

for Ti gtinv-351 potential where,

$$D^{(i)} = D_1^{(i)} \cup D_2^{(i)} \cup D_3^{(i)} \cup \cdots , \tag{3.16}$$

$$D_p^{(i)} = \{d^{(i)}_{nl_1l_2\cdots l_p}\}. \tag{3.17}$$

The lattice parameters for HCP and CTB which includes ten $\{10\bar{1}2\}$ layers with MLIP are shown in Table.3.1. These results agree well with those of DFT calculations shown in Chapter 2. Fig.3.6 shows phonon band structures and total DOSes for HCP and CTB structures in Mg and Ti. For Mg, phonon band structures and DOSes with MLIP potential are well reproduced with DFT calculations for both HCP and CTB structures. On the other hand, the agreement of band structures and DOSes for Ti is not so good as Mg, but still show the same shape features.

Table 3.1: Lattice parameters for HCP and CTB structures with MLIP and DFT calculations. For MLIP calculations, gtinv-883 for Mg and gtinv-351 for Ti are used. The twinning shears of the $\{10\bar{1}2\}$ twinning mode s^{t} are also shown.

		a^{h} [Å]	c^{h} [Å]	a [Å]	b [Å]	c [Å]	γ	s^{t}
Mg	MLIP	3.19	5.19	3.19	7.58	41.59	1.62	0.130
	DFT	3.19	5.19	3.19	7.58	41.60	1.63	0.126
Ti	MLIP	2.92	4.62	2.92	6.86	37.55	1.58	0.183
	DFT	2.94	4.65	2.94	6.89	37.74	1.58	0.181

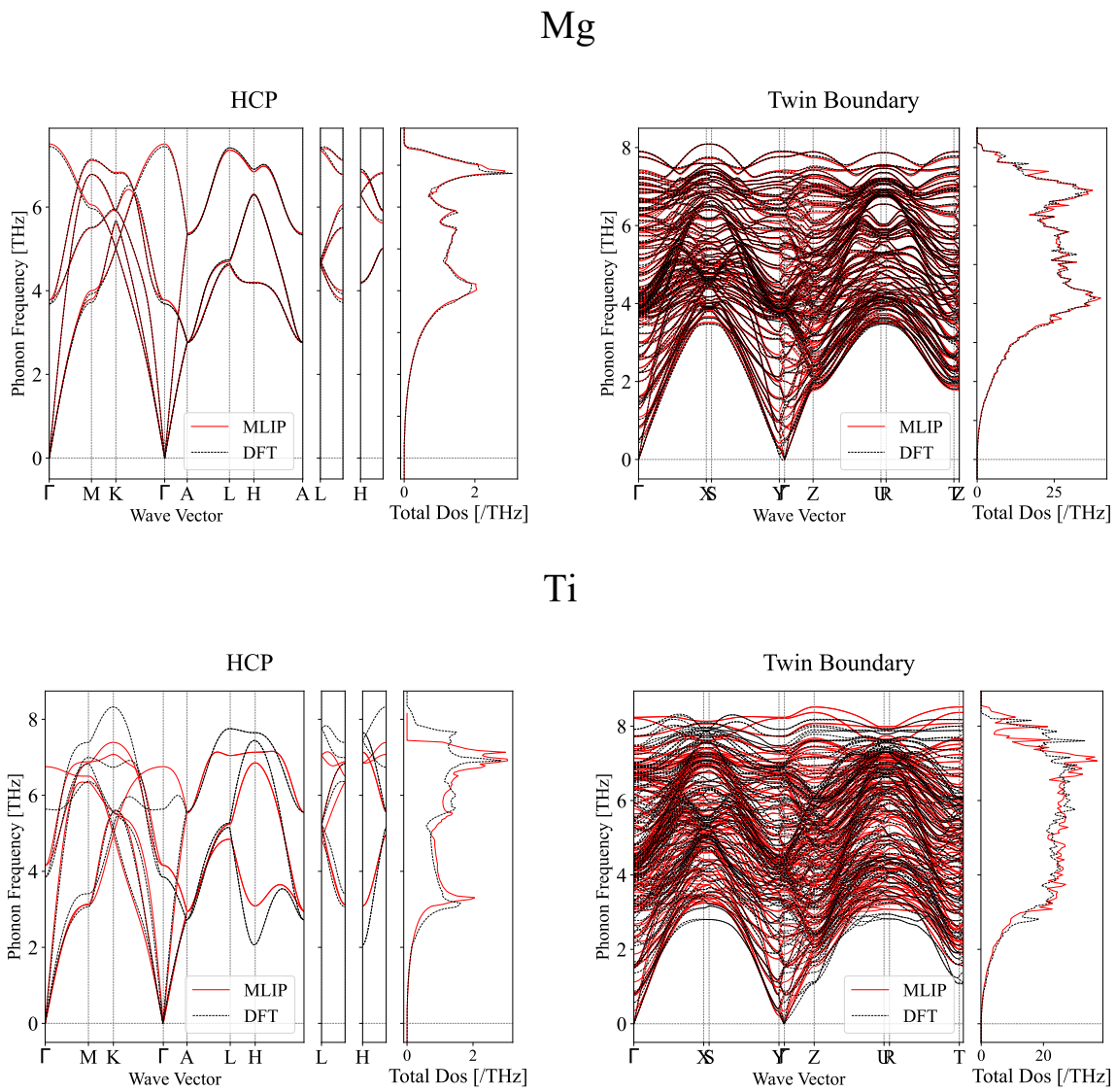

Figure 3.6: Phonon band structures and DOSes of HCP and CTB structures in Mg and Ti. Results from phonon calculations with MLIP and DFT are shown in red and black, respectively.

3.5 Results and discussions

As described in Section 3.2, three types of simulation cells were prepared where $n_z = 22$ and $n_y = \{29, 39, 49\}$ for Mg and Ti disconnection dipole introduced structures. For simplicity, we call

these structures as Type-1, Type-2 and Type-3 in order of the simulation cell size along y axis. The lattice parameters for disconnection structures in Mg and Ti for each structure type are shown in Table.3.2, The number of atoms in the simulation cells and the initial shear strains are also shown in the table.

Table 3.2: Lattice parameters for disconnection structures in Mg and Ti are shown. The number of atoms in the simulation cells and the initial shear strains are also shown in the table. For MLIP calculations, gtinv-883 for Mg and gtinv-351 for Ti were used.

	name	number of atoms	n_y	n_z	L [Å]	H [Å]	s^0
Mg	Type-1	1276	29	22	219.71	41.59	5.93×10^{-3}
	Type-2	1716	39	22	295.48	41.59	5.93×10^{-3}
	Type-3	2156	49	22	371.24	41.59	5.93×10^{-3}
Ti	Type-1	1276	29	22	198.83	37.55	8.33×10^{-3}
	Type-2	1716	39	22	267.39	37.55	8.33×10^{-3}
	Type-3	2156	49	22	335.95	37.55	8.33×10^{-3}

In Fig.3.7, Mg Type-1 structure after structure optimization with MLIP under the fixed lattice condition is shown as an example. The atomic colors are determined from common neighbor analysis (CNA) [50]. The red atoms indicate that the local atomic environment is categorized into HCP and the white atoms are neither FCC, BCC nor HCP. The disconnection introduced $\{10\bar{1}2\}$ twin boundary is indicated with the white atoms as shown in Fig.3.7. The theoretical background for CNA is described in Appendex A. During structure optimizations, the dual step did not move in all disconnection introduced structures in Mg and Ti.

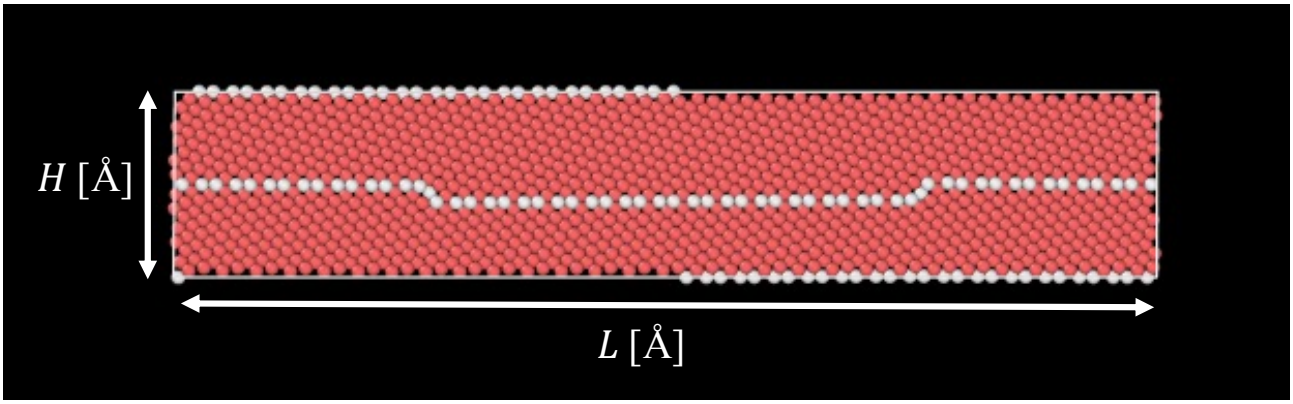

Figure 3.7: Mg Type-1 structure is shown. The atomic colors are determined from CNA. The red atoms represent the local atomic environment are categorized into HCP and the white atoms are neither FCC, BCC nor HCP. The dual step introduced $\{10\bar{1}2\}$ twin boundary is indicated with the white atoms as shown in the figure.

From the initial structure Type-1, Type-2 and Type-3 sheared by the initial shear strain s^0, the additional shear strains $s = \{\pm 1.0\times10^{-4}, \pm 2.0\times10^{-4}, \cdots, \pm 5.0\times10^{-3}\}$ were applied and structure optimizations were conducted. In Fig.3.8, the relations between shear strains and total energies and the relations between shear strains and shear stress σ_{yz} are shown. The results of $\{10\bar{1}2\}$ CTB structures in Mg and Ti using the molecular static calculations with MLIP are shown with black dots in Fig.3.8 as references. To compare the energies of the disconnection dipole introduced structures with the CTB structures, the total energies are divided by n_y, where $n_y = 1$ in CTB structures and the values of n_y are shown in Table.3.2 for Type-1, Type-2 and Type-3 structures in Mg and Ti. The total energy and shear stress changes in Mg and Ti CTB structures indicated with black dots are similar in that there are steps at $s = \pm 0,012$ for Mg $\{10\bar{1}2\}$ CTB structure and at $s = \pm 0.014$ for Ti $\{10\bar{1}2\}$ CTB structure. This steps represent the twin boundary migrations of CTB structures, where the twin grows two $\{10\bar{1}2\}$ layers at positive shear strain and the matrix grows two

$\{10\bar{1}2\}$ layers at negative shear strain. By the twin boundary migrations the total energies and shear stresses were decreased. This is similar with the twin boundary migrations based on first-principles phonon calculations shown in Chapter 2. However, the twin boundary migrations as a result of the molecular static calculations are not reliable because if we remember that atoms actually vibrate at finite temperature, the twin boundaries are expected to be migrate with smaller shear stress owing to the imaginary phonon mode as shown in Chapter 2. The total energies and shear stresses by adding shear strains of Type-1, Type-2 and Type-3, which are shown with red, blue and green lines in Fig.3.8, did not change so much at smaller shear strains from the initial shear strains s^0 both in Mg and Ti. At specific points they changes discontinuously and drop into the curve of CTB structures represented with black dots. This indicates the disconnection dipoles are disappeared and CTB structures are formed. From the results of total energy changes, the twin boundary migrations by the aid of disconnections occur with smaller energies compared with that of CTB both in Mg and Ti $\{10\bar{1}2\}$ twin boundaries.

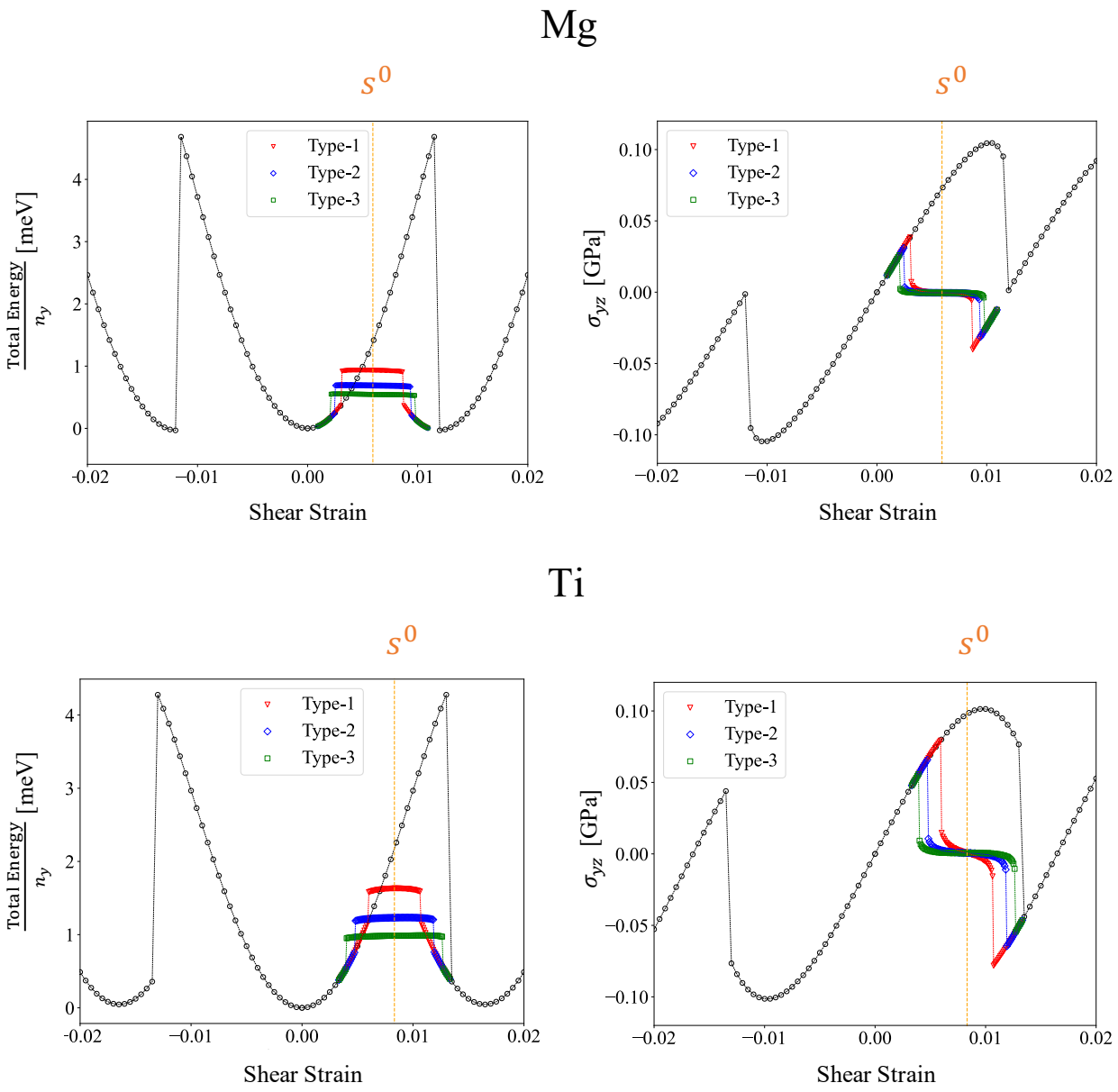

Figure 3.8: The relations between shear strains and total energies and the relations between shear strains and shear stresses σ_{yz} are shown. The results of $\{10\bar{1}2\}$ CTB structures in Mg and Ti are shown with black dots in Fig.3.8 as references. In order to compare the energies of the disconnection dipole introduced structures and the CTB structures, the total energies are divided by n_y, where $n_y = 1$ in CTB structures and the values of n_y are shown in Table.3.2 for Type-1, Type-2 and Type-3 structures in Mg and Ti.

Fig.3.9 shows the enlarged figures of the total energies of disconnection dipole introduced $\{10\bar{1}2\}$ twin boundaries in Mg and Ti. Note that the total energies shown in Fig.3.9 are not divided by n_y. From the figures, the formation energies of disconnections are independent from the simulation cell size and the values are about 26 meV for Mg and about 46 meV for Ti. The formation energy of Ti disconnection dipole is about two times larger than that of Mg.

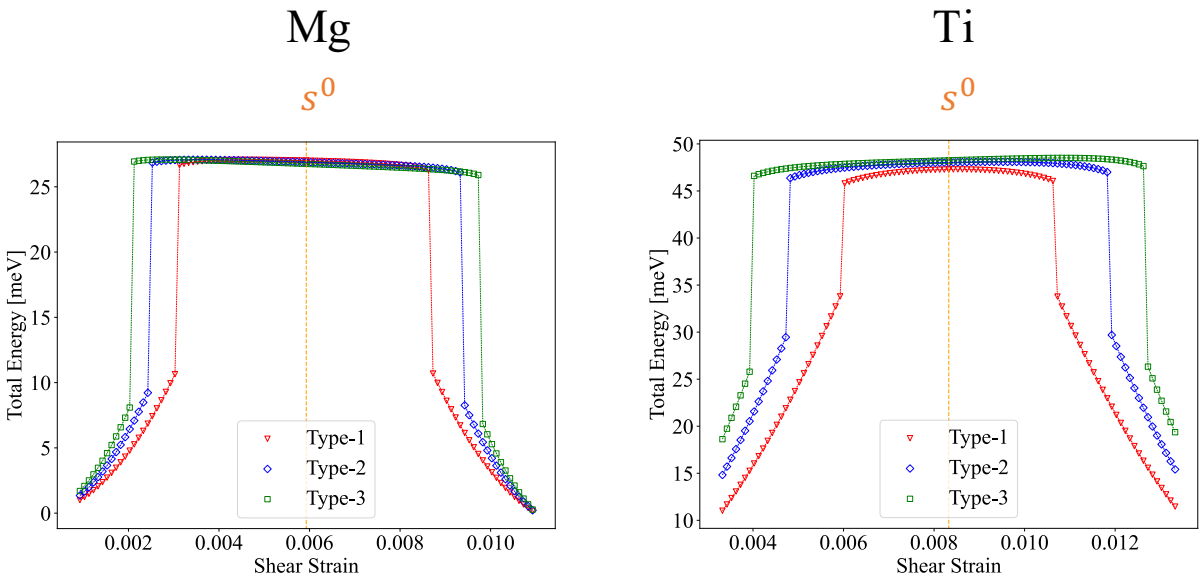

Figure 3.9: The total energies of Type-1, Type-2 and Type-3 structures in Mg and Ti. Note that the total energies shown in the figures are not divided by n_y.

Fig.3.10 is the enlarged figures of the shear stress σ_{yz} shown in Fig.3.8. With the smaller shear strain values from the initial shear strain s^0, the values of σ_{yz} are corrugated both in Mg and Ti. These corrugation become clear with larger simulation cells. Fig.3.11 shows the Mg Type-2 structures pointed with (a), (b) and (c) in Fig.3.8. (b) is the initial structure and (a) and (c) are the structures applied negative and positive shear strains. As shown in the figures, matrix

becomes large with negative shear strain and twin becomes large with positive shear strain both by disconnection dipole gliding on the twin boundary. Therefore, in the areas where the total energies change little as shown in Fig.3.8 around the initial shear strain s^0, disconnection dipole glides on the twin boundaries, and we need to get phonon structure changes in these areas for the discussion of atomic mechanism during twin boundary migrations.

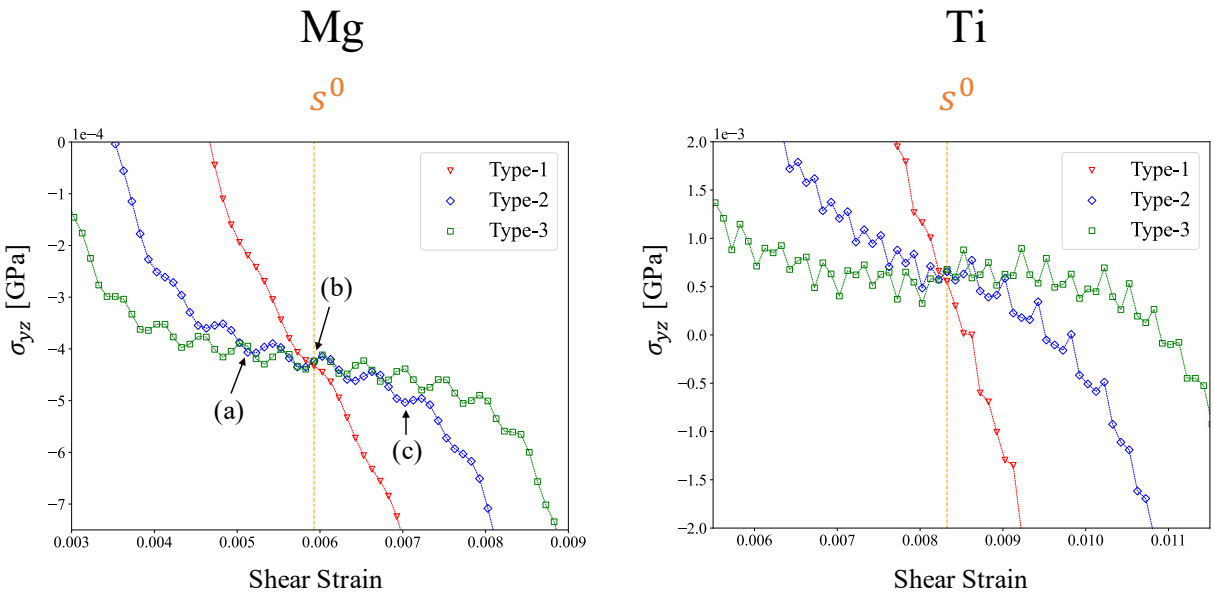

Figure 3.10: Enlarged views of the shear stress σ_{yz} shown in Fig.3.8. The structures pointed with (a), (b) and (c) in Mg Type-2 are shown in Fig.3.11.

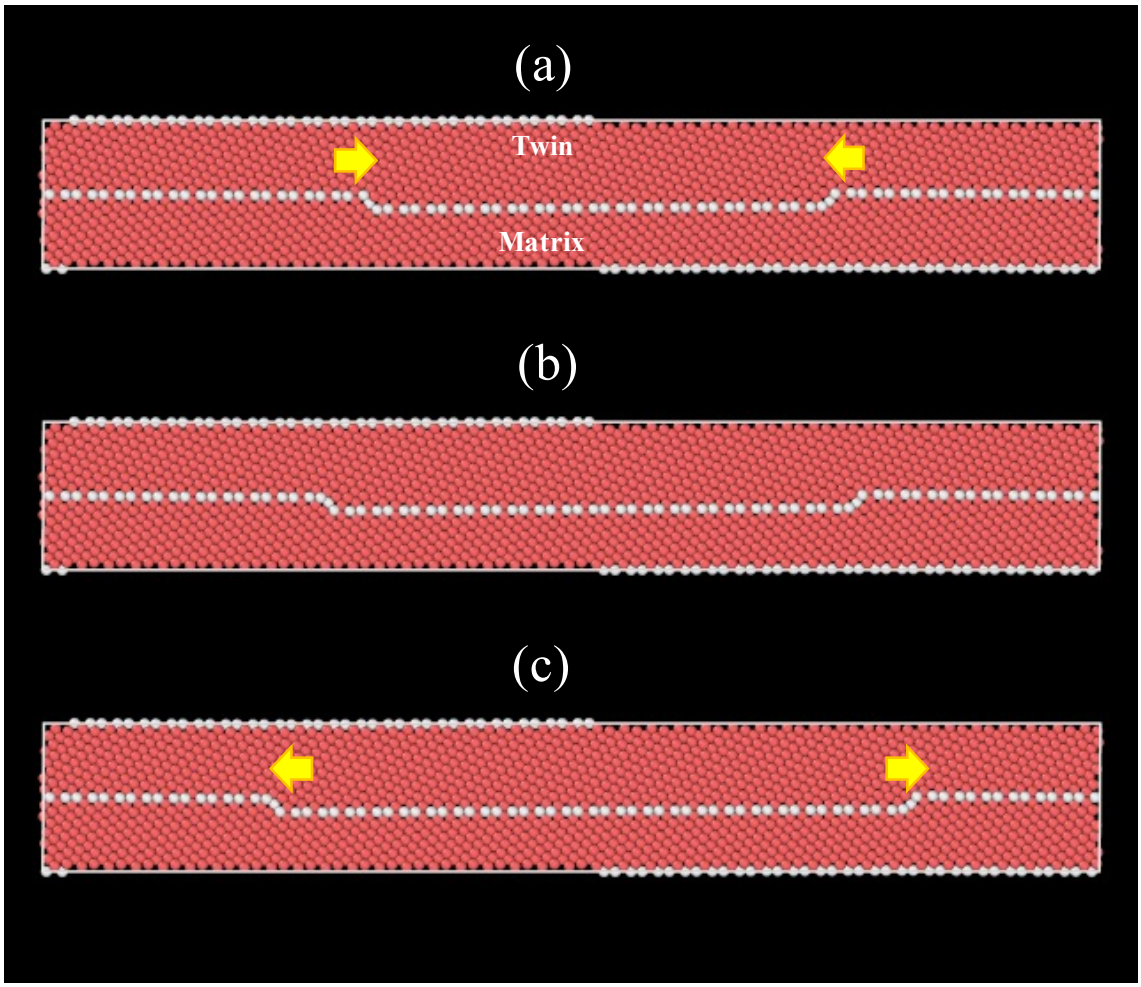

Figure 3.11: Mg Type-2 structures with different shear strain pointed with (a), (b) and (c) in Fig.3.8. Matrix becomes large with negative shear strain and twin becomes large with positive shear strain both by disconnection dipole gliding on the twin boundary as indicated with yellow arrows.

On the purpose of getting phonon structure changes during disconnection gliding on the twin boundaries, phonon calculations with MLIP were conducted toward the structures with the shear strains $s = \{0, \pm 1.0 \times 10^{-4}, \pm 2.0 \times 10^{-4}, \cdots, \pm 2.0 \times 10^{-3}\}$ from the initial shear strain s^0. Because of the large atomic numbers in the simulation cells, it is computationally too demanding to calculate phonons at multiple q-points for visualizing phonon dispersion curves and DOSes, we got phonons only at Γ point. Fig.3.12 and Fig.3.13 shows the phonon frequency changes at lowest ten phonon modes by applying shear stress of Type-1, Type-2 and Type-3 structures in Mg and Ti, respectively. Vertical orange lines indicate the initial shear strains s^0. In these figures, the three straight lines at 0 THz indicate acoustic modes because they have 0 THz of phonon frequencies at Γ point. Because we want to get the local atomic arrangement by a single disconnection gliding, the interactions between twin boundaries are preferred to be zero. By comparing different size simulation cells in Mg and Ti, the shape of the phonon frequency changes are similar and therefore, the interactions between twin boundaries can be expected negligible. As for optical modes, each phonon mode change the phonon frequency smoothly except the phonon mode which have the lowest phonon frequency indicated with red lines in each figure. In Mg, the changes of these phonon modes by shear strains are wavelike and periodic in Type-1, Type-2 and Type-3 structures. This indicates the local atomic arrangement of equilibrium positions around disconnection change periodically and the lowest optical phonon modes have largely affected this local atomic change. Moreover, because these phonon modes show imaginary phonon modes periodically, the simulation cells become dynamically unstable periodically. Therefore, based on lattice dynamics point of view, the initial structure becomes dynamically unstable periodically with shear strain, and the atomic rearrangement occurs owing to the emerged imaginary phonon modes. From this reason, it is clear that these lowest optical phonon modes play a central role in disconnection gliding along the twin boundaries. In Ti, the changes of the lowest optical phonon modes are not as clearly periodic as

that in Mg. However, the phonon frequencies of these phonon modes suddenly drop into imaginary mode at some shear strains. Therefore, these phonon modes also can be excepted to be the main factor of disconnection gliding.

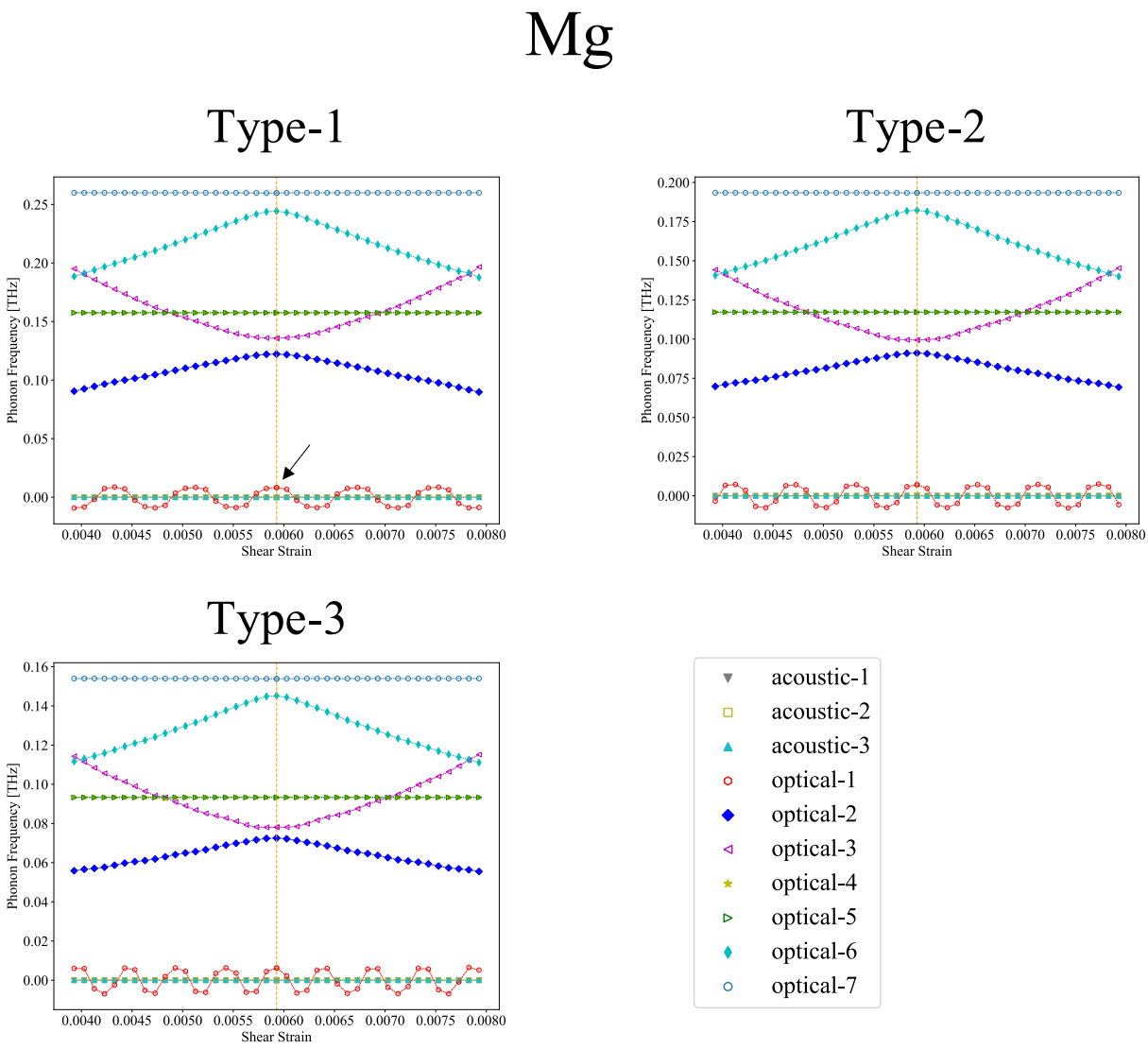

Figure 3.12: The phonon frequency changes at lowest ten phonon modes by applying shear stress of Type-1, Type-2 and Type-3 structures in Mg. The atomic displacements of the lowest optical phonon mode pointed with black arrow are shown in Fig.3.14.

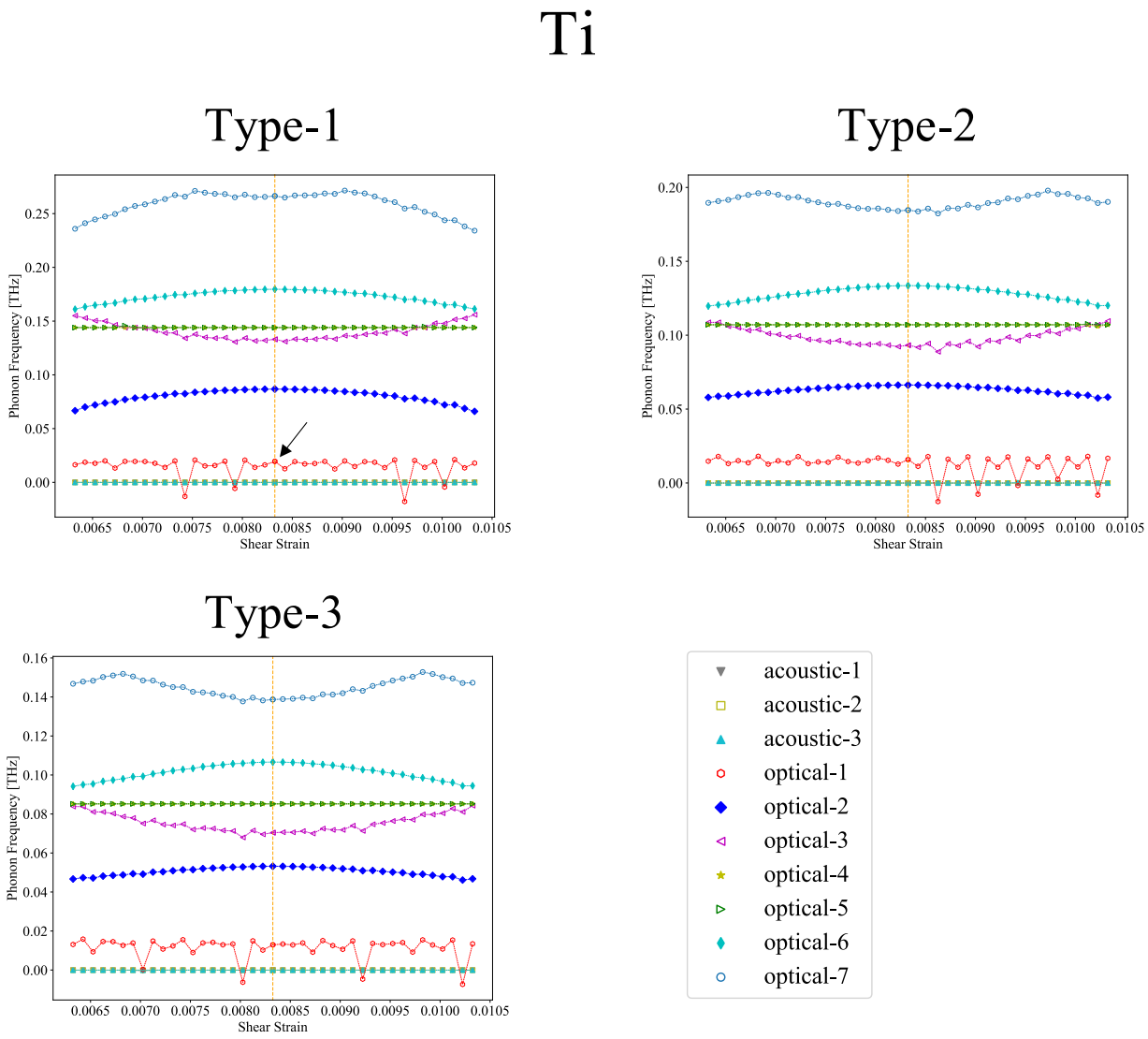

Figure 3.13: The phonon frequency changes at lowest ten phonon modes by applying shear stress of Type-1, Type-2 and Type-3 structures in Ti. The atomic displacements of the lowest optical phonon mode pointed with black arrow are shown in Fig.3.15.

In Fig.3.14 and Fig.3.15, the minimum optical phonon modes of Type-1 in Mg and Ti under the initial shear strain, which are indicated with black arrows in Fig.3.12 and Fig.3.13, are shown. The orange atoms in the figures indicate the atoms on the $\{10\bar{1}2\}$ twin boundaries. For visualization, the amplitudes are normalized in order that the largest amplitudes have 2 Å of the amplitudes. As shown in these figures, these two phonon modes show similar atomic vibrations. In both disconnection introduced structures, the atomic group rotation-like vibrations are shown at the disconnections indicated with blue round arrows. On the other hand, the atomic vibrations of the atoms on the twin boundary and far from the disconnections did not show rotation-like vibrations. This indicates if disconnection exists, the twin boundary migrations do not occur at CTB but occur around the dual step by disconnection gliding on the twin boundaries and this motions are owing to the imaginary phonon modes shown in Fig.3.12 and Fig.3.13.

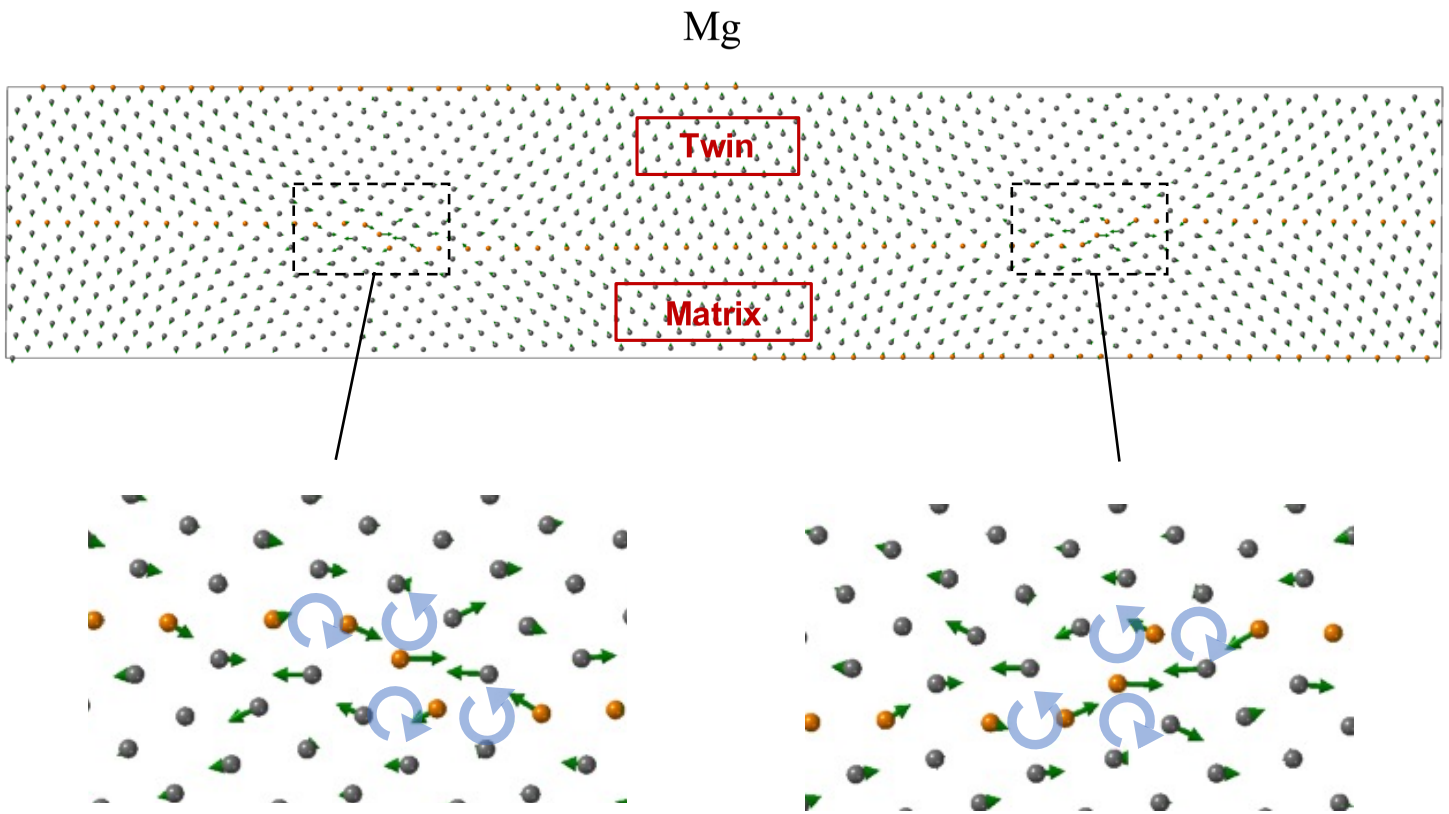

Figure 3.14: The atomic vibrations of the minimum optical phonon mode of Type-1 in Mg under the initial shear strain are shown. This phonon mode is indicated with black arrows in Fig.3.12. For visualization, the amplitudes are normalized in order that the largest amplitudes become 2 Å of the amplitudes. The atomic group rotation-like vibrations around the dual steps are indicated with blue round arrows.

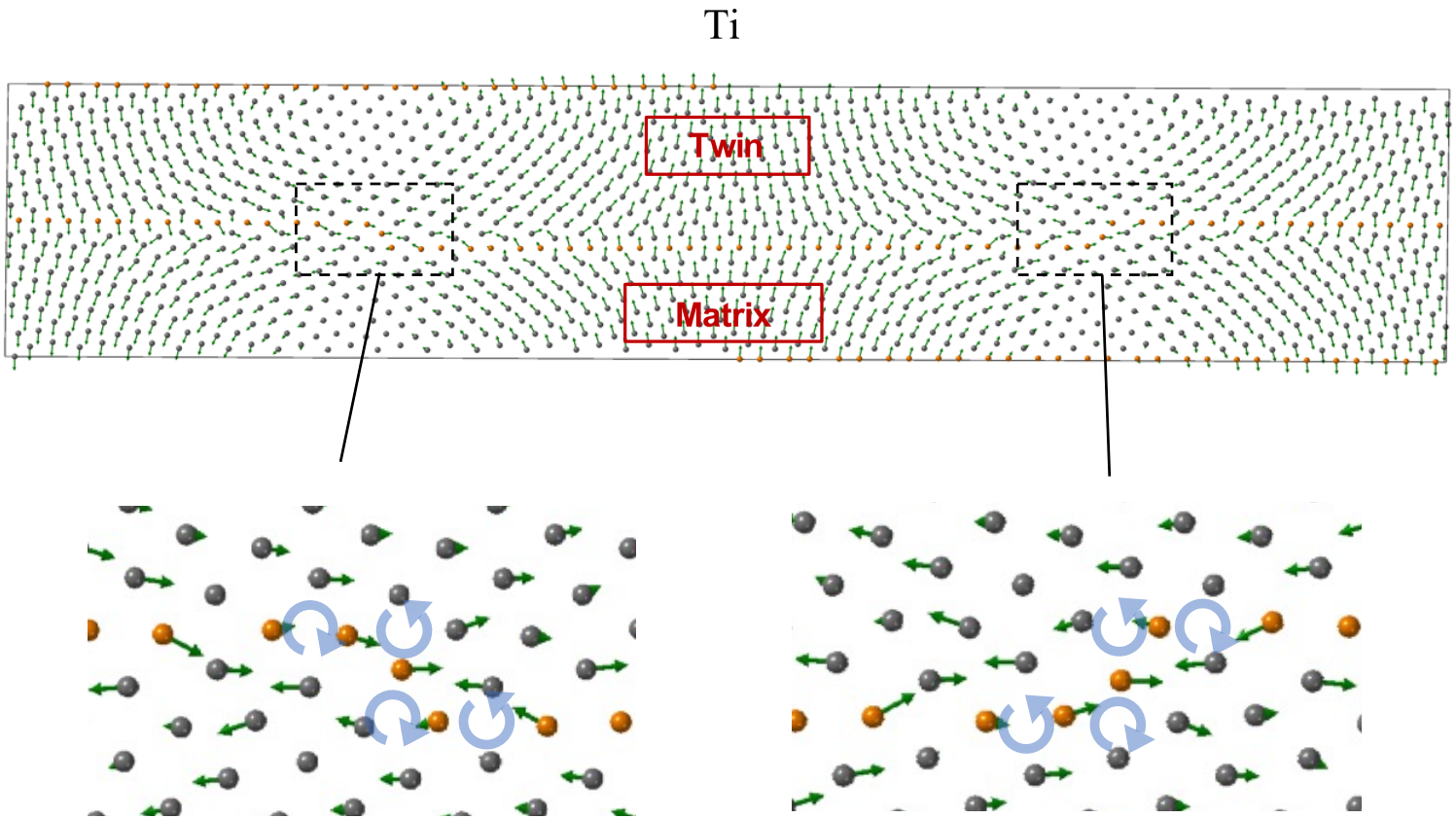

Figure 3.15: The atomic vibrations of the minimum optical phonon mode of Type-1 in Ti under the initial shear strain are shown. This phonon mode is indicated with black arrows in Fig.3.13. For visualization, the amplitudes are normalized in order that the largest amplitudes become 2 Å of the amplitudes. The atomic group rotation-like vibrations around the dual steps are indicated with blue round arrows.

3.6 Conclusion

In this chapter, we investigated the phonon structure changes of disconnection dipole introduced $\{10\bar{1}2\}$ structures in Mg and Ti. $\{10\bar{1}2\}$ twin boundary is actually not fully coherent but often deviates from theoretical one. Therefore, we considered more actual case and selected the dual step introduced twin boundary structures. This type of twin boundary has recently observed in Re $\{10\bar{1}2\}$ twin boundary with in-situ HRTEM. The dual steps meditated twin growth mechanism has been already proposed in 1996 with the concept "disconnection", which is interfacial defect exhibiting both dislocation and step character. However, this model does not provide the driving force for disconnection gliding and the atomic trajectories during twin growth based on energetic point of view. From these backgrounds, we decided to investigate the atomic rearrangement associated with the disconnection gliding.

Disconnection introduced twin boundary structures were built from dichromatic patterns and corresponding macroscopic shear strains were added. Because of the large simulation cells which contain more than a thousand of atoms, it was computationally impossible to conduct phonon calculations with first-principles. Therefore, we used machine learning interatomic potential (MLIP) for all structure optimization and phonon calculations. The phonon calculations for HCP and CTB structures with selected MLIPs were well reproduced with first-principles phonon calculations. After checking the accuracy of MLIP toward phonon calculations, we conducted a series of phonon calculations toward shear strain applied disconnection structures in Mg and Ti. As a result, we found the characteristic optical phonon modes which have the smallest phonon frequencies at Γ point. Their phonon frequencies are changed periodically between positive and negative phonon frequencies by external shear stress. Therefore, the disconnection introduced structures periodically become dynamically unstable, which indicate these phonon modes trigger the disconnection

gliding. To conform this, the characteristic phonon modes were visualized. These phonon modes were very similar in that the atomic vibration directions were the same between Mg and Ti. The atomic vibration directions around disconnections were rotation-like where the atomic vibrations of the atoms on the twin boundaries and far from disconnections did not show rotation-like vibrations. Therefore, we can conclude that if disconnection exists, the twin boundary migrations occur by disconnection gliding on the twin boundaries and the corresponding atomic rearrangement is characterized by the smallest optical phonon modes which become periodically the imaginary phonon modes.

Chapter 4

General Conclusion

In this thesis, we revealed the phonon structures of Mg and Ti $\{10\bar{1}2\}$ twin boundaries and their changes with external shear stresses and provided atomic rearrangement mechanism of twin growth by a series of phonon calculations.

In Chapter 2, we investigated the phonon structure changes in Mg and Ti $\{10\bar{1}2\}$ CTB structures associated with applying external shear stresses by first-principles phonon calculations. Both Mg and Ti $\{10\bar{1}2\}$ CTB structures did not show the imaginary phonon mode under zero shear stress conditions. By adding shear strain to the CTB structures, the imaginary phonon modes were emerged at Γ point. Because the imaginary phonon modes indicate the sheared CTB structures are dynamically unstable, we investigated the atomic rearrangement mechanism using the eigenvectors of these imaginary phonon modes. As a result, the twin boundary migrations were occurred both in Mg and Ti associated with atomic rotation-like rearrangement around twin boundaries. From this result, we concluded when external shear stress is added to the $\{10\bar{1}2\}$ CTBs, the atomic group rotation-like rearrangement around twin boundary occurs triggered by the imaginary phonon mode and this results in twin boundary migration.

In Chapter 3, we investigated the phonon structure changes of disconnection dipole introduced

$\{10\bar{1}2\}$ twin boundary structures in Mg and Ti as a more actual case by phonon calculations with MLIP. We conducted a series of phonon calculations toward shear strain applied disconnection structures in Mg and Ti. As a result, we found the characteristic optical phonon modes which have the smallest phonon frequencies at Γ point both in Mg and Ti. Because these phonon modes dropped into the imaginary by external shear stresses, we considered them as the triggers for disconnection gliding and the atomic vibration directions were visualized using their eigenvectors. As a result, the atomic vibration directions around disconnection were rotation-like where the atomic vibrations of the atoms on the twin boundaries and far from disconnections did not show rotation-like vibrations. Therefore, we concluded that if disconnection exists, the twin boundary migrations occur by disconnection gliding on the twin boundaries and the corresponding atomic rearrangement is characterized the smallest optical phonon modes which become periodically the imaginary phonon modes.

In conclusion, we revealed the atomic scale rearrangement mechanism during twin growth in Mg and Ti. In twin growth of CTB structures and disconnection introduced $\{10\bar{1}2\}$ twin boundaries, atomic rotation-like rearrangement was the main factor for twin boundary migrations. As shown in this thesis, phonon analysis based on lattice dynamics is effective to study the local atomic rearrangement process such as twin growth. We expect that the atomic mechanism of twin growth in the other deformation twinning modes and the twin nucleation from grain boundary can be unraveled with the same approach as used in this thesis.

Appendix A

Common Neighbor Analysis

In this appendix, we review the methodology of common neighbor analysis (CNA) which first proposed by [50], implemented to computer 3D graphics by [67], and well summarized by [68]. CNA is one of the popular local structure analysis methods and allows to identify atoms in particular environment, such as FCC, BCC and HCP from atomic pair distances in the vast and complexed atomic scale simulation systems.

In CNA, cutoff distance is the only given parameters. When a specific atomic pair i and j is focused, the atoms within the cutoff distance from both i and j atoms are considered to be "common neighbors" marked with k in Fig.A.1. Each atomic pair is classified by a set of four indices from the relations among these atoms. The first index is 1 or 2 which indicates that a specific atomic pair i and j are the neighbors or not. The second index represent the number of common neighbors which are shared by atoms i and j. The third index indicates the number of bonds among the common neighbors. The forth index differentiates diagrams with the same first three indices and with different bonding patterns among common neighbors. For example, the diagrams (a) and (b) in Fig.A.1 have the same first three indices, but the bonding patterns of common neighbor atoms labeled with k are different, where two bonds bridging common neighbor atoms are separated in

(a) but these bonds are connected via one of the common neighbor atoms in (b). The local atomic environment of the atom i is determined by relative presence of the labels for a set of atomic pairs where one of them is atom i. If the relative presence is matched with that of a structure type shown in Table.A.1, the local environment of atom i is separated into the matched structure type.

Throughout this thesis, 3.85 Å and 3.47 Å of cutoff radii were used for Mg and Ti, respectively.

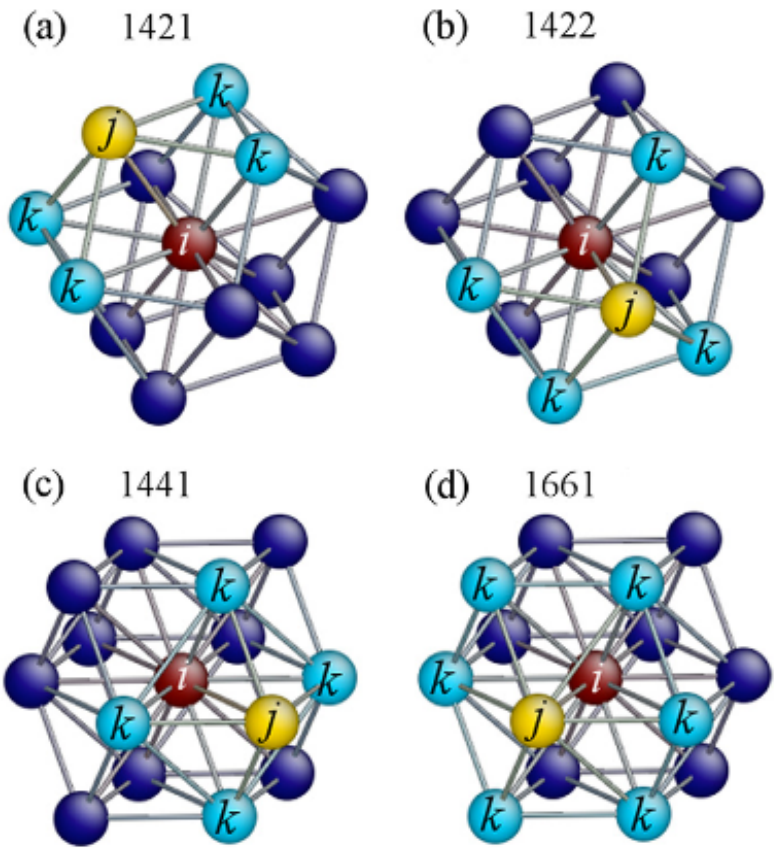

Figure A.1: Illustrations of diagrams constructed from the classification of local structures defined in the CNA method visualized by Tsuzuki *et al.* [68]. Four-digit numbers represent the atomic environment of the pair of brown atom i and yellow atom j in each diagram. They share the atoms k as neighbor atoms, which are called as common neighbors.

Table A.1: Relative presence of different CNA diagrams in FCC, BCC and HCP crystal structures shown by Tsuzuki *et al.* in his paper [68].

CNA diagram	FCC	BCC	HCP
1421	1	0	1/2
1422	0	0	1/2
1441	0	3/7	0
1661	0	4/7	0

Bibliography

[1] Kulekci, M. K. Magnesium and its alloys applications in automotive industry. *The International Journal of Advanced Manufacturing Technology* **39**, 851–865 (2008).

[2] Hanson, B. Present and future uses of titanium in engineering. *Materials & Design* **7**, 301–307 (1986).

[3] Burke, E. C. & Hibbard, W. R. Plastic Deformation of Magnesium Single Crystals. *JOM* **4**, 295–303 (1952).

[4] Farenc, S., Caillard, D. & Couret, A. An in situ study of prismatic glide in α titanium at low temperatures. *Acta Metallurgica et Materialia* **41**, 2701–2709 (1993).

[5] Britton, T. B., Dunne, F. P. E. & Wilkinson, A. J. On the mechanistic basis of deformation at the microscale in hexagonal close-packed metals. *Proceedings of the Royal Society A: Mathematical, Physical and Engineering Sciences* **471**, 20140881 (2015).

[6] Bilby, B. A. & Crocker, A. G. The theory of the crystallography of deformation twinning. *Proceedings of the Royal Society of London. Series A. Mathematical and Physical Sciences* **288**, 240–255 (1965).

[7] Christian, J. & Mahajan, S. Deformation twinning. *Progress in Materials Science* **39**, 1–157 (1995).

[8] Yoo, M. H. Slip, twinning, and fracture in hexagonal close-packed metals. *Metallurgical Transactions A* **12**, 409–418 (1981).

[9] Yu, Q. *et al.* Twin–twin interactions in magnesium. *Acta Materialia* **77**, 28–42 (2014).

[10] Xu, S. *et al.* Sequential {10-12} twinning stimulated by other twins in titanium. *Acta Materialia* **132**, 57–68 (2017).

[11] Hirth, J. & Pond, R. Steps, dislocations and disconnections as interface defects relating to structure and phase transformations. *Acta Materialia* **44**, 4749–4763 (1996).

[12] Serra, A. & Bacon, D. J. A new model for 1012 twin growth in hcp metals. *Philosophical Magazine A* **73**, 333–343 (1996).

[13] Li, B. & Ma, E. Atomic Shuffling Dominated Mechanism for Deformation Twinning in Magnesium. *Physical Review Letters* **103**, 035503 (2009).

[14] Yu, S., Liu, C., Gao, Y., Jiang, S. & Chen, Z. A rotation-shear model on the atomic motion during {10-12} twinning in magnesium alloys. *Materials Letters* **165**, 185–188 (2016).

[15] Cayron, C. Hard-sphere displacive model of extension twinning in magnesium. *Materials & Design* **119**, 361–375 (2017).

[16] Jiang, S., Jiang, Z. & Chen, Q. Deformation twinning mechanism in hexagonal-close-packed crystals. *Scientific Reports* **9**, 618 (2019).

[17] Sun, Q., Zhang, X., Ren, Y., Tu, J. & Liu, Q. Interfacial structure of {10-12} twin tip in deformed magnesium alloy. *Scripta Materialia* **90–91**, 41–44 (2014).

[18] Sun, Q. *et al.* Characterization of basal-prismatic interface of twin in deformed titanium by high-resolution transmission electron microscopy. *Philosophical Magazine Letters* **95**, 145–151 (2015).

[19] He, Y., Li, B., Wang, C. & Mao, S. X. Direct observation of dual-step twinning nucleation in hexagonal close-packed crystals. *Nature Communications* **11**, 2483 (2020).

[20] Togo, A., Inoue, Y. & Tanaka, I. Phonon structure of titanium under shear deformation along {101-2} twinning mode. *Physical Review B* **102**, 024106 (2020).

[21] Pond, R. C. & Vlachavas, D. S. Bicrystallography. *Proceedings of the Royal Society of London. A. Mathematical and Physical Sciences* **386**, 95–143 (1983).

[22] Kresse, G. & Hafner, J. Ab initio molecular dynamics for liquid metals. *Physical Review B* **47**, 558–561 (1993).

[23] Kresse, G. & Hafner, J. Ab initio molecular-dynamics simulation of the liquid-metal–amorphous-semiconductor transition in germanium. *Physical Review B* **49**, 14251–14269 (1994).

[24] Kresse, G. & Furthmüller, J. Efficiency of ab-initio total energy calculations for metals and semiconductors using a plane-wave basis set. *Computational Materials Science* **6**, 15–50 (1996).

[25] Kresse, G. & Furthmüller, J. Efficient iterative schemes for ab initio total-energy calculations using a plane-wave basis set. *Physical Review B* **54**, 11169–11186 (1996).

[26] Togo, A. & Tanaka, I. First principles phonon calculations in materials science. *Scripta Materialia* **108**, 1–5 (2015).

[27] Pei, Z. *et al.* Atomic structures of twin boundaries in hexagonal close-packed metallic crystals with particular focus on Mg. *npj Computational Materials* **3**, 1–7 (2017).

[28] Pei, Z., Sheng, H., Zhang, X., Li, R. & Svendsen, B. Tunable twin stability and an accurate magnesium interatomic potential for dislocation-twin interactions. *Materials & Design* **153**, 232–241 (2018).

[29] Bhatia, M. A. & Solanki, K. N. Energetics of vacancy segregation to symmetric tilt grain boundaries in hexagonal closed pack materials. *Journal of Applied Physics* **114**, 244309 (2013).

[30] Wang, J. & Beyerlein, I. J. Atomic structures of symmetric tilt grain boundaries in hexagonal close packed (hcp) crystals. *Modelling and Simulation in Materials Science and Engineering* **20**, 024002 (2012).

[31] Kumar, A., Wang, J. & Tomé, C. First-principles study of energy and atomic solubility of twinning-associated boundaries in hexagonal metals. *Acta Materialia* **85**, 144–154 (2015).

[32] Zhang, J., Dou, Y. & Zheng, Y. Twin-boundary segregation energies and solute-diffusion activation enthalpies in Mg-based binary systems: A first-principles study. *Scripta Materialia* **80**, 17–20 (2014).

[33] Tsuru, T., Somekawa, H. & Chrzan, D. Interfacial segregation and fracture in Mg-based binary alloys: Experimental and first-principles perspective. *Acta Materialia* **151**, 78–86 (2018).

[34] Qian, Q. *et al.* Basal stacking fault induced twin boundary gliding, twinning disconnection and twin growth in hcp Ti from the first-principles. *Transactions of Nonferrous Metals Society of China* **31**, 382–390 (2021).

[35] Hall, E. O. *Twinning and Diffusionless Transformations in Metals* (Butterworths Scientific Publications, London, 1954).

[36] Pond, R. C. & Bollmann, W. The symmetry and interfacial structure of bicrystals. *Philosophical Transactions of the Royal Society of London. Series A, Mathematical and Physical Sciences* **292**, 449–472 (1979).

[37] Ostapovets, A. & Serra, A. Review of Non-Classical Features of Deformation Twinning in hcp Metals and Their Description by Disconnection Mechanisms. *Metals* **10**, 1134 (2020).

[38] Wallace, D. C. & Callen, H. Thermodynamics of Crystals. *American Journal of Physics* **40**, 1718–1719 (1972).

[39] Dove, M. T. *Introduction to Lattice Dynamics* (Cambridge University Press, 1993), first edn.

[40] Ziman, J. *Electrons and Phonons* (Oxford University Press, 2001).

[41] Srivastava, G. P. *The Physics of Phonons* (Routledge, 2019), first edn.

[42] Moriwake, H. *et al.* First-principles calculations of lattice dynamics in CdTiO3 and CaTiO3 : Phase stability and ferroelectricity. *Physical Review B* **84**, 104114 (2011).

[43] Blöchl, P. E. Projector augmented-wave method. *Physical Review B* **50**, 17953–17979 (1994).

[44] Perdew, J. P., Burke, K. & Ernzerhof, M. Generalized Gradient Approximation Made Simple. *Physical Review Letters* **77**, 3865–3868 (1996).

[45] Methfessel, M. & Paxton, A. T. High-precision sampling for Brillouin-zone integration in metals. *Physical Review B* **40**, 3616–3621 (1989).

[46] Kresse, G., Furthmüller, J. & Hafner, J. *Ab Initio* Force Constant Approach to Phonon Dispersion Relations of Diamond and Graphite. *Europhysics Letters (EPL)* **32**, 729–734 (1995).

[47] Uhrin, M., Huber, S. P., Yu, J., Marzari, N. & Pizzi, G. Workflows in AiiDA: Engineering a high-throughput, event-based engine for robust and modular computational workflows. *Computational Materials Science* **187**, 110086 (2021).

[48] Togo, A. & Tanaka, I. $\texttt{Spglib}$: A software library for crystal symmetry search. *arXiv:1808.01590 [cond-mat]* (2018). 1808.01590.

[49] Hinuma, Y., Pizzi, G., Kumagai, Y., Oba, F. & Tanaka, I. Band structure diagram paths based on crystallography. *Computational Materials Science* **128**, 140–184 (2017).

[50] Honeycutt, J. D. & Andersen, H. C. Molecular dynamics study of melting and freezing of small Lennard-Jones clusters. *The Journal of Physical Chemistry* **91**, 4950–4963 (1987).

[51] Stukowski, A. Visualization and analysis of atomistic simulation data with OVITO the Open Visualization Tool. *Modelling and Simulation in Materials Science and Engineering* **18**, 015012 (2010).

[52] Ostapovets, A. & Gröger, R. Twinning disconnections and basal–prismatic twin boundary in magnesium. *Modelling and Simulation in Materials Science and Engineering* **22**, 025015 (2014).

[53] Wang, J., Hirth, J. & Tomé, C. $(1\bar{0}12)$ Twinning nucleation mechanisms in hexagonal-close-packed crystals. *Acta Materialia* **57**, 5521–5530 (2009).

[54] Ostapovets, A. & Serra, A. Slip dislocation and twin nucleation mechanisms in hcp metals. *Journal of Materials Science* **52**, 533–540 (2017).

[55] MacKain, O., Cottura, M., Rodney, D. & Clouet, E. Atomic-scale modeling of twinning disconnections in zirconium. *Physical Review B* **95**, 134102 (2017).

[56] Martínez, E., Capolungo, L. & Tomé, C. N. Atomistic analysis of the {10-12} twin stability and growth in α -Ti. *Physical Review Materials* **2**, 083603 (2018).

[57] Serra, A., Kvashin, N. & Anento, N. On the common topological conditions for shear-coupled twin boundary migration in bcc and hcp metals. *Letters on Materials* **10**, 537–542 (2020).

[58] Wang, S., Dang, K., McCabe, R. J., Capolungo, L. & Tomé, C. N. Three-dimensional atomic scale characterization of { 11 2 $\bar{}$ 2 } twin boundaries in titanium. *Acta Materialia* **208**, 116707 (2021).

[59] Khater, H., Serra, A. & Pond, R. Atomic shearing and shuffling accompanying the motion of twinning disconnections in Zirconium. *Philosophical Magazine* **93**, 1279–1298 (2013).

[60] Pond, R. C., Hirth, J. P., Serra, A. & Bacon, D. J. Atomic displacements accompanying deformation twinning: Shears and shuffles. *Materials Research Letters* **4**, 185–190 (2016).

[61] Seko, A., Togo, A. & Tanaka, I. Group-theoretical high-order rotational invariants for structural representations: Application to linearized machine learning interatomic potential. *Physical Review B* **99**, 214108 (2019).

[62] Seko, A. Machine learning potentials for multicomponent systems: The Ti-Al binary system. *Physical Review B* **102**, 174104 (2020).

[63] El-Batanouny, M. & Wooten, F. *Symmetry and Condensed Matter Physics: A Computational Approach* (Cambridge University Press, Cambridge, 2008).

[64] Thompson, A. P. *et al.* LAMMPS - a flexible simulation tool for particle-based materials modeling at the atomic, meso, and continuum scales. *Computer Physics Communications* **271**, 108171 (2022).

[65] Levin, I. NIST Inorganic Crystal Structure Database (ICSD) (2020).

[66] Branke, J., Deb, K., Miettinen, K. & Słowiński, R. (eds.) *Multiobjective Optimization: Interactive and Evolutionary Approaches*, vol. 5252 of *Lecture Notes in Computer Science* (Springer Berlin Heidelberg, Berlin, Heidelberg, 2008).

[67] Faken, D. & Jónsson, H. Systematic analysis of local atomic structure combined with 3D computer graphics. *Computational Materials Science* **2**, 279–286 (1994).

[68] Tsuzuki, H., Branicio, P. S. & Rino, J. P. Structural characterization of deformed crystals by analysis of common atomic neighborhood. *Computer Physics Communications* **177**, 518–523 (2007).

Acknowledgement

The author would like to express the deepest gratitude to Professor Isao Tanaka at Ktoto University for continuous guidance, support and encouragement throughout the three years of his research in Doctor course. The author sincerely thanks to Dr. Atsushi Togo for generous discussions and advice for first-principles phonon calculations. The author wishes to express his deep gratitude to Professor Haruyuki Inui and Professor Hiroyuki Nakamura for carefully reading this dissertation and offering suggestions. The author acknowledges Associate Professor Atsuto Seko and Assistant Professor Hiroyuki Hayashi for their productive advice on the research work. The author also greatly appreciates the kindness of Ms. Makiko Orita for the management of the research activities. The author would like to express his sincerely thanks to the whole members of Tanaka laboratory and to the Kyoto University for offering the great research environment.

Finally, the author would like to sincerely thank his family for their enduring support and encouragement.